Modeling Evaporation in the Rarefied Gas Regime
by using Macroscopic Transport Equations

by

Alexander Felix Beckmann
B.Sc., University of Hannover, 2014

A Thesis Submitted in Partial Fulfillment of the
Requirements for the Degree of

MASTER OF APPLIED SCIENCE

in the Department of Mechanical Engineering

Modeling Evaporation in the Rarefied Gas Regime
by using Macroscopic Transport Equations

by

Alexander Felix Beckmann
B.Sc., University of Hannover, 2014

Supervisory Committee

Dr. H. Struchtrup, Supervisor
(Department of Mechanical Engineering)

Dr. B. Buckham, Departmental Member
(Department of Mechanical Engineering)

Supervisory Committee

Dr. H. Struchtrup, Supervisor
(Department of Mechanical Engineering)

Dr. B. Buckham, Departmental Member
(Department of Mechanical Engineering)

ABSTRACT

Due to failure of the continuum hypothesis for higher Knudsen numbers, rarefied gases and microflows of gases are particularly difficult to model. Macroscopic transport equations compete with particle methods, such as the direct simulation Monte Carlo method (DSMC) to find accurate solutions in the rarefied gas regime. Due to growing interest in micro flow applications, such as micro fuel cells, it is important to model and understand evaporation in this flow regime.

To gain a better understanding of evaporation physics, a non-steady simulation for slow evaporation in a microscopic system, based on the Navier-Stokes-Fourier equations, is conducted. The one-dimensional problem consists of a liquid and vapor layer (both pure water) with respective heights of 0.1mm and a corresponding Knudsen number of Kn=0.01, where vapor is pumped out. The simulation allows for calculation of the evaporation rate within both the transient process and in steady state.

The main contribution of this work is the derivation of new evaporation boundary conditions for the R13 equations, which are macroscopic transport equations with proven applicability in the transition regime. The approach for deriving the boundary conditions is based on an entropy balance, which is integrated around the liquid-vapor interface. The new equations utilize Onsager relations, linear relations between thermodynamic fluxes and forces, with constant coefficients that need to be determined. For this, the boundary conditions are fitted to DSMC data and compared to other

R13 boundary conditions from kinetic theory and Navier-Stokes-Fourier solutions for two steady-state, one-dimensional problems. Overall, the suggested fittings of the new phenomenological boundary conditions show better agreement to DSMC than the alternative kinetic theory evaporation boundary conditions for R13.

Furthermore, the new evaporation boundary conditions for R13 are implemented in a code for the numerical solution of complex, two-dimensional geometries and compared to Navier-Stokes-Fourier (NSF) solutions. Different flow patterns between R13 and NSF for higher Knudsen numbers are observed which suggest continuation of this work.

Contents

List of Tables

List of Figures

ACKNOWLEDGEMENTS

I want to express my deepest gratitude to Prof. Henning Struchtrup, for guiding and encouraging me throughout the past years. I highly appreciate how much time he took for teaching his students and me. I deeply acknowledge the encouragement and support from Prof. Kabelac (University of Hannover, Germany) to conduct my Master program in Canada. Also, I want to thank Prof. Torrilhon for the opportunity to do research in collaboration with the RWTH Aachen University, Germany.

I want to thank my colleagues and friends Behnam Rahimi, Samira Soltani, Alireza Mohammadzadeh and Devesh Bharadwaj who warmly welcomed me in their research group.

My deepest gratitude goes to my parents and my sister Katharina for their support and love.

I sincerely acknowledge the funding from Natural Sciences and Engineering Research Council (NSERC) of Canada.

DEDICATION

I dedicate this work to my sister Katharina, my mother Sabine and my father Helmut, whom I can always rely on.

Chapter 1

Introduction

The phase change between liquid and vapor plays an important role in many technical processes. Often this phase change is desired such as in refrigeration cycles where evaporators remove heat from a cold reservoir and condensers reject heat to the environment [1][2]. In steam power plants liquid water is evaporated, then expanded in a turbine and eventually condensed again [2][3][4]. In other applications, evaporation or condensation may occur which is not desired. Water management plays an important role in fuel cell systems [5][6] and having control over the phase of the water is crucial for optimal operation.

When developing new technologies, it is desired to compare mathematical models with experimental data where the mathematical approach is by far cheaper.

Modeling evaporation and condensation has been subject of research for the past century. However, previous work has been mostly concerned with a flow regime, where the equations of classical hydrodynamics, i.e., the Navier-Stokes-Fourier equations are valid. Though, there are many applications where the continuum hypothesis and therefore classical hydrodynamics fail, such as flow within micro electro mechanical devices (MEMS) [7] or vacuum applications.

The present work starts with modeling slow evaporation in a microscopic system where classical hydrodynamics are just valid (Chap. 2). The results give insight into the physics of evaporation. In Chap. 3 macroscopic transport equations with applicability in flow regimes beyond the scope of classical hydrodynamics are extended by deriving new evaporation/condensation boundary conditions. These boundary conditions utilize coefficients which are determined by fitting to reference data for a half-space and a finite problem. In Chap. 4 the newly derived boundary conditions are put to test in a numerical steady-state simulation for complex geometries. The

work ends with the conclusion and outlook in Chap. 5.

1.1 Microscopic vs. macroscopic approach

For modeling ideal gas flow, there are in general two approaches, the microscopic and the macroscopic approach. In the microscopic approach, the Boltzmann equation [8][9] is solved, e.g., with the Direct Simulation Monte Carlo method (DSMC) [10]. By neglecting external forces, the Boltzmann equation is given as

$$\frac{\partial f}{\partial t} + c_k \frac{\partial f}{\partial x_k} = \frac{1}{Kn} S(f) = \frac{1}{Kn} \int_0^{2\pi} \int_0^{\pi/2} \left(f' f^{1'} - f f^1 \right) g \sigma_c \sin\theta d\theta d\epsilon d\mathbf{c}^1 \ , \tag{1.1}$$

with $f(x_k, c_k, t)$ as single particle distribution function, in which $x_k = \{x_1, x_x, x_3\}$ is the position vector and $c_k = \{c_1, c_2, c_3\}$ the vector denoting microscopic velocity. The term $S(f)$ describes binary collisions between particles and, if set to zero, Eq. (1.1) describes free flight. The distribution function $f(x_k, c_k, t)$ is defined over the relation $N_{x_k, c_k} = f(x_k, c_k, t) dx_k dc_k$ which is the number of particles within a cell of phase space $dx_k dc_k$ at time t [9][11]. The collision term $S(f)$ consists of $f = f(x_k, c_k, t)$ and $f^1 = f(x_k, c_k^1, t)$, which denote the respective distribution of the two incoming particles before collision, $f' = f(x_k, c_k', t)$ and $f^{1'} = f(x_k, c_k^{1'}, t)$ as distribution of outgoing particles after collision, θ as the collision angle, ϵ as the orientation of the collision plane, σ_c as the differential cross section and g as the relative velocity of the incoming particles.

By knowing the distribution function one may condense microscopic information into macroscopic quantities which are also referred to as moments. Some moments of the distribution function are given as

$$\text{Mass density: } \rho = m \int f d\mathbf{c} \ , \tag{1.2}$$

$$\text{Velocity: } \rho v_i = m \int c_i f d\mathbf{c} \ , \tag{1.3}$$

$$\text{Internal energy: } \rho u = \frac{3}{2} \rho \theta = \frac{m}{2} \int C^2 f d\mathbf{c} \ , \tag{1.4}$$

$$\text{Pressure tensor: } p_{ij} = p\delta_{ij} + \sigma_{ij} = m \int C_i C_j f d\mathbf{c} \ , \tag{1.5}$$

$$\text{Stress tensor: } \sigma_{ij} = m \int C_{\langle i} C_{j \rangle} f d\mathbf{c} \ , \tag{1.6}$$

$$\text{Heat flux vector: } q_i = \frac{m}{2} \int C^2 C_i f d\mathbf{c} \ . \tag{1.7}$$

The ideal gas law is here defined as $p = \rho\theta$, with $\theta = RT$ and the peculiar velocity as

$$C_i = c_i - v_i \ , \tag{1.8}$$

in which c_i is the microscopic velocity and v_i the bulk velocity, def. (1.3). Indices in angular brackets denote trace free and symmetric tensors.

The Boltzmann equation is difficult and computationally expensive to solve and for engineering applications determining the macroscopic quantities only is often sufficient. In the macroscopic approach, sets of equations, e.g., the Navier-Stokes-Fourier equations (classical hydrodynamics) are derived from the Boltzmann equation. These equations reduce the number of variables, and when simplified, allow for analytical solutions. The advantage of faster calculations is associated with the restriction to certain flow regimes [12].

1.2 Characteristics of micro and rarefied gas flow

Macroscopic transport equations approximate the Boltzmann equation (1.1) and are bound to certain flow regimes, which can be characterized by the Knudsen number. The Knudsen number is the ratio of the mean free path, i.e., the average distance a molecule travels between two subsequent collisions, and a characteristic length, e.g. the diameter of a pipe [11]. The Knudsen number is defined as

$$\mathrm{Kn} = \frac{\mu\sqrt{RT}}{pL} \ , \tag{1.9}$$

with μ as dynamic viscosity, L as characteristic length, R as individual gas constant, T as temperature and $p = \rho RT$ as pressure. For Knudsen numbers larger than $\mathrm{Kn} \approx 4 \cdot 10^{-2}$ the classical Navier-Stokes-Fourier equations (NSF) start to fail [11][12]. Applications for Knudsen numbers in the transition regime, i.e., $4 \cdot 10^{-2} < \mathrm{Kn} < 2.5$ [12], may be those with large mean free paths, e.g., in vacuum or aerospace applications, or those with small characteristic lengths, which can be found in microflows. In this regime rarefaction effects are observed, such as temperature jump and velocity

slip at interfaces, Knudsen layers in front of interfaces, transpiration flow, thermal stresses, or heat transfer without temperature gradients [11][12][13][14][15]. Knudsen layers are thin areas in front of boundaries in the order of a few mean free paths, which correspond to a discontinuity between the phase density right at the boundary, where particle interaction with the boundary is the dominant mechanism and the phase density for the bulk flow.

1.3 The Navier-Stokes-Fourier equations

As first approach for modeling evaporation one considers the Navier-Stokes-Fourier equations (NSF) from classical fluid mechanics, which are valid for relatively small Knudsen numbers only. For a fluid (liquid or gas) the conservation laws in local form for mass, momentum and energy are given as [16]

$$\frac{\partial \rho}{\partial t} + \frac{\partial \rho v_k}{\partial x_k} = 0 \ , \tag{1.10}$$

$$\frac{\partial \rho v_i}{\partial t} + \frac{\partial \rho v_i v_k + p_{ik}}{\partial x_k} = \rho g_i \ , \tag{1.11}$$

$$\frac{\partial \rho \left(u + \frac{v^2}{2}\right)}{\partial t} + \frac{\partial \left(\rho \left(u + \frac{v^2}{2}\right) v_k + p_{ik} v_i + q_k\right)}{\partial x_k} = \rho g_i v_i \ , \tag{1.12}$$

in which $p_{ik} = p\delta_{ik} + \sigma_{ik}$ is the pressure tensor, with δ_{ik} as identity matrix. The tensor notation is used in which the symbol for sum is neglected, i.e., $\sum_{k=1}^{3} \frac{\partial v_k}{\partial x_k} = \frac{\partial v_k}{\partial x_k}$. Here, ρ is mass density, v_i velocity vector, u specific internal energy, p pressure, σ_{ik} viscous stress tensor, q_k conductive heat flux vector and g_i a body force, e.g., gravitational force. The variables depend on the position vector x_k, which for three dimensions in space reads $x_k = \{x_1, x_2, x_3\}$ and time t. One has five equations for the five unknowns ρ, v_i and T. An algebraic equation for p is found in the ideal gas law $p = \rho RT$. To close the system, it is necessary to find equations for q_k and σ_{ik} which are given by Fourier's law

$$q_k = -k \frac{\partial T}{\partial x_k} \ , \tag{1.13}$$

and the Navier-Stokes stress tensor for a compressible fluid, with superscript v for vapor as [16]

$$\sigma_{ik}^{v} = -\mu \left[\frac{\partial v_i}{\partial x_k} + \frac{\partial v_k}{\partial x_i} - \frac{2}{3} \frac{\partial v_j}{\partial x_j} \delta_{ik} \right] - \nu \frac{\partial v_j}{\partial x_j} \delta_{ik} \ , \tag{1.14}$$

in which μ is the dynamic viscosity and ν the bulk viscosity. When considering a monatomic gas, the bulk viscosity becomes zero.

For an incompressible and Newtonian liquid the divergence $\frac{\partial v_j}{\partial x_j}$ is zero and therefore the stress tensor simplifies to

$$\sigma_{ik}^{l} = -\mu \left[\frac{\partial v_i}{\partial x_k} + \frac{\partial v_k}{\partial x_i} \right] \ . \tag{1.15}$$

Under the assumption of constant specific heats, the equation of state for enthalpy in vapor is

$$h_v = c_v^p \left(T_v - T_0 \right) + h_{gl}^0 \ , \tag{1.16}$$

with $h_{gl}^0 = h_g^0 - h_l^0$, see Appendix A. One notes, that if the equilibrium temperature T_0 is not set to zero, one obtains $h_v(T_0) = h_{gl}^0$, which appears convenient. However, since enthalpy differences are considered, the choice of T_0 does not effect the results eventually. After combination with $u_v = h_v - \frac{p_v}{\rho_v}$ and the ideal gas law, Eq. (1.16) becomes

$$u_v = T_v(c_v^p - R) + h_{gl}^0 - T_0 c_v^p \ . \tag{1.17}$$

For an incompressible fluid, the equation of state for enthalpy reads

$$h_l = c_l^p (T_l - T_0) + \frac{1}{\rho_l} \left(p_l - p_{l0} \right) \ , \tag{1.18}$$

and by using the definition for internal energy $u_l = h_l - \frac{p_l}{\rho_l}$ it follows

$$u_l = c_l^p (T_l - T_0) - \frac{p_{l0}}{\rho_l} \ . \tag{1.19}$$

By using the appropriate stress tensor, Eq. (1.14) or (1.15), and equations of state, NSF can be used to model liquid or vapor. Modeling evaporation is mainly a matter of the corresponding interface or boundary conditions between liquid and vapor which are discussed in the next chapters.

Chapter 2

A Transient Simulation on Evaporation

2.1 1-D, Non-steady evaporation problem

To gain an insight into the physics of evaporation processes, the Navier-Stokes-Equations (NSF), Eqs. (1.10-1.12) are considered. The system of interest, depicted in Fig. 2.1, consists of a liquid and a vapor layer divided by an interface. Equilib-

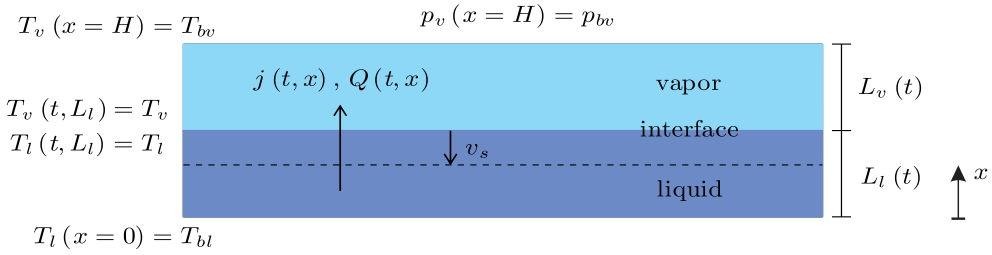

Figure 2.1: Evaporation in one-dimensional and non-steady state system.

rium pressure of the system, when no evaporation occurs, is the saturation pressure at temperature T_0, $p_0 = p_{sat}\,(T_0)$. The driving force of evaporation is the controlled pressure at the top boundary

$$p_v(x = H) = p_{bv}\ , \tag{2.1}$$

which is set to $p_{bv} < p_0$. Simply speaking, vapor is pumped out of the top boundary which decreases the pressure at every location in the system and therefore forces evaporation. As result, mass and convective heat (j and Q) are transferred from

Equilibrium pressure:	$p_0 = p_{sat}\,(298K) = 3169Pa$
Vaporization enthalpy:	$h^0_{gl}\,(298K) = 2442.3 \cdot 10^3 \frac{J}{kg}$
Specific gas constant:	$R = 461.9 \frac{J}{kgK}$
Density vapor:	$\rho_{v0} = \frac{p_0}{RT_0}$
Density liquid:	$\rho_l = 1000 \frac{kg}{m^3}$
Isobaric specific heat vapor:	$c^p_v = \frac{5}{2}R$
Specific heat liquid:	$c_l = 4180 \frac{J}{kgK}$
Thermal conductivity vapor:	$k_v = 0.014 \frac{W}{mK}$
Thermal conductivity liquid:	$k_l = 0.55 \frac{W}{mK}$

Table 2.1: Material properties for water.

vapor velocity	$v_v(x,0) = 0$
vapor pressure	$p_v(x,0) = p_0 = p_{sat}\,(T_0)$
liquid pressure	$p_l(x,0) = p_0 = p_{sat}\,(T_0)$
temperature	$T_l(x,0) = T_v(x,0) = T_0$
position interface	$L_l(t=0) = L_{l0}$

Table 2.2: Initial conditions for non-steady evaporation system.

liquid to vapor and out of the system at $x = H$. The choice of equilibrium pressure allows for small differences between p_{bv} and p_0 to start evaporation. Additionally the temperatures on bottom and top

$$T_l(x=0) = T_{bl} = const. \quad , \tag{2.2}$$

$$T_v(x=H) = T_{bv} = const. \quad , \tag{2.3}$$

are controlled and if not set to T_0, evaporation can be driven by them as well. The liquid layer is at rest ($v_l = 0$) while being depleted, as a result the interface moves into the negative x direction with velocity v_s. The controlled boundary conditions, Eqs. (2.1-2.3) are chosen to be constant in time. The system is much wider than it is high, which minimizes impact of left and right boundaries and allows for a one-dimensional description. The interface is assumed to be an infinitesimal thin volume by letting its height approach zero, $\Delta x \to 0$. Material properties for water are taken out of Table 2.1. The initial conditions ($t = 0$) are depicted in Table 2.2. It is desired to obtain a full thermodynamic solution of the system with simplified NSF.

2.2 Simplification of NSF equations for one-dimensional system

For heat and mass transfer for one dimension in space, the mass- and momentum balances (1.10, 1.11) for the vapor bulk become

$$\frac{\partial \rho_v}{\partial t} + \frac{\partial \rho_v v_v}{\partial x} = 0 \ , \tag{2.4}$$

$$\frac{\partial \rho_v v_v}{\partial t} + \frac{\partial}{\partial x}\left(\rho_v v_v^2 + p - \sigma_{11}\right) = \rho_v f_1 \ , \tag{2.5}$$

with the simplified compressible stress tensor (1.14) as

$$\sigma_{11} = \left(\frac{4}{3}\mu + \nu\right)\frac{\partial v}{\partial x} \ . \tag{2.6}$$

The momentum balance for vapor is further simplified by neglecting gravitation, which is justified due to low mass density of vapor. The square of velocity is neglected due to slow fluid flow and also the stress tensor which, relative to temperature or density, is assumed to have a small impact in the present system. Then the momentum balance reduces to

$$\frac{\partial \rho_v v_v}{\partial t} + R\frac{\partial \rho_v T_v}{\partial x} = 0 \ , \tag{2.7}$$

where the ideal gas law $p = \rho RT$ was introduced. The one-dimensional energy balance for vapor reads

$$\frac{\partial \rho_v \left(u_v + \frac{1}{2}v_v^2\right)}{\partial t} + \frac{\partial}{\partial x}\left(\rho_v\left(u_v + \frac{1}{2}v_v^2\right)v_v + p_v + q_v - \sigma_{11}v_v\right) = \rho_v f_1 v_v \ . \tag{2.8}$$

With the same assumptions as the momentum balance, the energy balance can be reduced to

$$\frac{\partial \rho_v u_v}{\partial t} + \frac{\partial}{\partial x}\left(v_v h_v \rho_v + q_v\right) = 0 \ , \tag{2.9}$$

where $h = u + \frac{p}{\rho}$ was introduced. By using Eq. (1.17) together with Fourier's heat conduction, Eq. (1.13), and under the assumption of constant thermal conductivity k_v, the energy balance for vapor becomes

$$(c_v^p - R)\frac{\partial \rho_v T_v}{\partial t} + c_v^p \frac{\partial v_v \rho_v T_v}{\partial x} - k_v \frac{\partial^2 T_v}{\partial x^2} = 0 \ . \tag{2.10}$$

	vapor	liquid
mass	$\frac{\partial \rho_v}{\partial t} + \frac{\partial \rho_v v_v}{\partial x} = 0$	$\frac{\partial v_l}{\partial x} = 0$
momentum	$\frac{\partial \rho_v v_v}{\partial t} + R\frac{\partial \rho_v T_v}{\partial x} = 0$	$\frac{\partial p_l}{\partial x} = 0$
energy	$(c_v^p - R)\frac{\partial \rho_v T_v}{\partial t} + c_v^p \frac{\partial v_v \rho_v T_v}{\partial x} - k_v \frac{\partial^2 T_v}{\partial x^2} = 0$	$\rho_l c_l \frac{\partial T_l}{\partial t} - k_l \frac{\partial^2 T_l}{\partial x^2} = 0$

Table 2.3: Simplified Navier-Stokes-Fourier equations for non-steady evaporation system.

With constant density, the mass balance of the liquid layer reads

$$\frac{\partial v_l}{\partial x} = 0 \ . \tag{2.11}$$

By recalling, that the liquid is it rest, and under the same assumptions as for the momentum balance for vapor (2.5), the momentum balance for liquid simplifies to

$$\frac{\partial p_l}{\partial x} = 0 \ , \tag{2.12}$$

which may be integrated trivially and leads to constant pressure $p_l = const.$ in the liquid layer. The gravitational force and therefore the hydrostatic pressure is neglected by considering a thin liquid layer. By taking into account all previous stated assumptions and with Eq. (1.13), the energy balance for liquid becomes

$$\rho_l \frac{\partial u_l}{\partial t} + \frac{\partial q_l}{\partial x} = 0 \ , \tag{2.13}$$

and by using Eq. (1.19), it further simplifies to

$$\rho_l c_l^p \frac{\partial T_l}{\partial t} - k_l \frac{\partial^2 T_l}{\partial x^2} = 0 \ . \tag{2.14}$$

The bulk equations for liquid and vapor are summarized in Table 2.3.

2.2.1 Linearization and non-dimensionalization of NSF

Linearizing around an equilibrium state defined over temperature T_0, density ρ_0 and pressure $p_0 = p_{sat}(T_0)$ allows for further simplification of the bulk equations as stated in Table 2.3. The equations below describe the relation between dimensionless deviation to equilibrium (overbar) and regular variables

$$T = T_0\left(1+\overline{T}\right), \quad \rho = \rho_0\left(1+\overline{\rho}\right), \quad p = p_0\left(1+\overline{p}\right) \ , \tag{2.15}$$

$$x_k = L\overline{x}_k, \quad t = \frac{L}{v_0}\bar{t}, \quad v_k = v_0\overline{v}_k \ .$$

The equations in Table 2.3 are modified by applying (2.15) and ignoring all terms, which are non-linear in the deviations to equilibrium. This method is based on the dimensionless deviations (close to equilibrium) being represented by a value N with $-1 < N < 1$, so that multiplication with other deviations always leads to a product, which is smaller than any of the factors. All variables are non-dimensional and describe the deviation from the equilibrium state. Hence, mass and momentum balances in the vapor become

$$\frac{\partial\overline{\rho}_v}{\partial\overline{t}} + \frac{\partial\overline{v}_v}{\partial\overline{x}} = 0 \ , \tag{2.16}$$

$$\frac{v_0^2}{RT_0}\frac{\partial\overline{v}}{\partial\overline{t}} + \frac{\partial\overline{T}}{\partial\overline{x}} + \frac{\partial\overline{\rho}}{\partial\overline{x}} = 0 \ . \tag{2.17}$$

The factor RT_0 in (2.17) has the same order of magnitude as the speed of sound which for an ideal gas can be written as $a = \sqrt{\kappa RT_v}$, with $\kappa = \frac{c_p}{c_v}$. Slow evaporation in the order of magnitude of $v_0 = 1\frac{m}{s}$ is assumed and therefore $\frac{v_0^2}{RT_0} \ll 1$. This allows to neglect the time derivative in (2.17). For obtaining a simple solution it is desired to decouple the equations in Table 2.3 as much as possible. Note, that in the solution later on, the time and velocity scale is changed, where $v_0 = \sqrt{RT_0}$ was used. Hence the momentum balance in vapor becomes

$$\frac{\partial\left(\overline{T}_v + \overline{\rho}_v\right)}{\partial\overline{x}} = 0 \ , \tag{2.18}$$

which after integration reads

$$\overline{T}_v + \overline{\rho}_v = C(t) = \overline{p}(x=H,t) = \overline{p}_{bv}(t) \quad \text{or} \quad \overline{\rho}_v = \overline{p}_{bv}(t) - \overline{T}_v \ . \tag{2.19}$$

The ideal gas law, which in linearized and non-dimensional form (deviation from equilibrium), assumes the form $\overline{\rho}_v = -\overline{T}_v + \overline{p}_v$ and is used to eliminate density in the momentum balance for vapor (2.18), which after integration becomes

$$\overline{p}_v = \overline{p}_{bv} \ . \tag{2.20}$$

With Eqs. (2.12) and (2.20), the pressure in the entire system is constant and equal to the controlled pressure p_{bv} on the top boundary. The integrated momentum balance for vapor (2.19) is plugged into the mass balance (2.16) and with $\frac{\partial p_{bv}(t)}{\partial \bar{t}} = 0$ the modified mass balance for vapor becomes

$$\frac{\partial \overline{T}_v}{\partial \bar{t}} - \frac{\partial \overline{v}_v}{\partial \overline{x}} = 0 \ . \tag{2.21}$$

The energy balance for vapor (2.10) after linearization and non-dimensionalization reads

$$-R\frac{\partial \overline{\rho}_v}{\partial \bar{t}} + (c_v^p - R)\frac{\partial \overline{T}_v}{\partial \bar{t}} - \frac{k_v}{\rho_{v0} v_0 L}\frac{\partial^2 \overline{T}_v}{\partial \overline{x}^2} = 0 \ . \tag{2.22}$$

By using the integrated momentum balance, Eq. (2.19) again, the energy balance for vapor becomes

$$\frac{\partial \overline{T}_v}{\partial \bar{t}} - k_v \frac{RT_0}{c_v^p p_0 v_0 L}\frac{\partial^2 \overline{T}_v}{\partial \overline{x}^2} = 0 \ . \tag{2.23}$$

Having the temperature as unknown only, the discussed simplifications decouple the energy balance from momentum and mass balances and make it therefore simple to solve. Finally, the mass balance (2.21) is combined with the energy balance (2.23) to find

$$\frac{\partial \overline{v}_v}{\partial \overline{x}} - k_v \frac{RT_0}{c_v^p p_0 v_0 L}\frac{\partial^2 \overline{T}_v}{\partial \overline{x}^2} = 0 \ . \tag{2.24}$$

After integration, Eq. (2.24) allows to calculate the vapor velocity $v_v(x,t)$ depending on vapor temperature T_v without the issue of solving a time derivative. Mass and momentum balances of liquid, Eq. (2.11) and (2.12) do not change their appearance in linear and dimensionless form. The energy balance for liquid (2.14) slightly changes in linearized and non-dimensional form and reads

$$\frac{\partial \overline{T}_l}{\partial \bar{t}} - \frac{k_l}{L\rho_l c_l v_0}\frac{\partial^2 \overline{T}_l}{\partial \overline{x}^2} = 0 \ . \tag{2.25}$$

A summary of the Navier-Stokes-Fourier equations, simplified, linearized and in non-

	vapor	liquid
mass	$\frac{\partial \overline{v}_v}{\partial \overline{x}} - k_v \frac{RT_0}{c_v^p p_0 v_0 L} \frac{\partial^2 \overline{T}_v}{\partial \overline{x}^2} = 0$	$\frac{\partial \overline{v_l}}{\partial x} = 0$
momentum	$\frac{\partial \overline{p}_v}{\partial \overline{x}} = 0$	$\frac{\partial \overline{p_l}}{\partial x} = 0$
energy	$\frac{\partial \overline{T}_v}{\partial \overline{t}} - k_v \frac{RT_0}{c_v^p p_0 v_0 L} \frac{\partial^2 \overline{T}_v}{\partial \overline{x}^2} = 0$	$\frac{\partial \overline{T}_l}{\partial \overline{t}} - \frac{k_l}{L \rho_l c_l v_0} \frac{\partial^2 \overline{T}_l}{\partial \overline{x}^2} = 0$

Table 2.4: Simplified, linearized and non-dimensional Navier-Stokes-Fourier equations for unsteady evaporation system.

dimensional form is given in Table 2.4.

2.3 Defining and simplifying the boundary conditions

For integrating the equations in Table 2.4, boundary conditions and interface conditions for velocity, pressure and two temperatures for both vapor and liquid are required. Three boundary conditions are found in Eqs. (2.1-2.3) by controlling temperatures at both boundaries and pressure at $x = H$. The mass balance (1.10) is integrated around an interface between liquid and vapor and becomes

$$\rho_l \widehat{v}_l^{L_l} = \rho_v^{L_l} \widehat{v}_v^{L_l} \ , \tag{2.26}$$

with the liquid and vapor velocities $\widehat{v}_l^{L_l}$ and $\widehat{v}_v^{L_l}$ at location L_l from the perspective of an observer moving with the interface. By using Galilei transformation one obtains

$$\widehat{v}_v^{L_l} - \widehat{v}_l^{L_l} = v_v^{L_l} - v_l^{L_l} \ , \tag{2.27}$$

with $v_\alpha^{L_l}$ as velocities observed from a laboratory reference frame. The liquid is at rest so that $v_l^{L_l} = 0$. The liquid reservoir is depleted by evaporation and the interface between liquid and vapor moves towards $x = 0$, with velocity $v_s = \frac{dL_l}{dt}$. The relative liquid velocity from an observer moving with the interface is found by observation as

$$\widehat{v}_l^{L_l} = -\frac{dL_l}{dt} = -v_s \ . \tag{2.28}$$

For Eq. (2.27) follows

$$\widehat{v}_v^{L_l} = v_v^{L_l} - \frac{dL_l}{dt} \ . \tag{2.29}$$

Eq. (2.28) and (2.27) are substituted into the integrated mass balance for vapor (2.26), which then becomes

$$\frac{dL_l}{dt} = \frac{\rho_v^{L_l} v_v^{L_l}}{\rho_v^{L_l} - \rho_l} \ . \tag{2.30}$$

The momentum balance (1.11) integrated around the interface reads

$$\rho_l^{L_l} \widehat{v}_l^{L_l} \widehat{v}_l^{L_l} + p_l^{L_l} = \rho_v^{L_v} \widehat{v}_v^{L_v} \widehat{v}_v^{L_v} + p_v^{L_l} \ . \tag{2.31}$$

Again the square of velocity is neglected so that

$$p_l^{L_l} = p_v^{L_l} \ . \tag{2.32}$$

The energy balance, Eq. (1.12) integrated around an interface between liquid and vapor reads

$$\rho_l \widehat{v}_l^{L_l} h_l + q_l^{L_l} = \rho_v^{L_l} \widehat{v}_v^{L_l} h_v + q_v^{L_l} \ . \tag{2.33}$$

For simplicity it is desired to use velocities from the laboratory reference frame. The integrated energy balance (2.33) is manipulated by using Eqs. (2.28, 2.29), heat conduction according to Fourier (1.13), the caloric equations of state, (1.16) and (1.18), and the integrated mass balance (2.26). It follows

$$\frac{\partial T_l^{L_l}}{\partial x} = -\frac{1}{k_l} \left(\begin{array}{c} \left(c_v^p \left(T_v - T_o\right) + h_{gl}^0\right) \rho_v^{L_l} v_v^{L_l} + \\ + \left(\left(-c_v^p T_v + c_v^p T_0 - h_{gl}^0\right) \rho_v^{L_l} + \rho_l c_l \left(T_l - T_0\right)\right) \left(\frac{\rho_v^{L_l} v_v^{L_l}}{\rho_v^{L_l} - \rho_l}\right) - k_v \frac{\partial T_v^{L_l}}{\partial x} \end{array} \right) \ . \tag{2.34}$$

Two evaporation interface conditions are found over the Onsager theory, which utilizes an integrated entropy balance [17][18]:

$$\frac{p_{sat}^{L_l} - p_v^{L_l}}{\sqrt{2\pi R T_l^{L_l}}} = \widehat{r}_{11} j^{L_l} + \widehat{r}_{12} \frac{q_v^{L_l}}{R T_l^{L_l}} \ , \tag{2.35}$$

$$-\frac{p_{sat}^{L_l}}{\sqrt{2\pi R T_l}} \frac{\left(T_v^{L_l} - T_l^{L_l}\right)}{T_l^{L_l}} = \widehat{r}_{21} j^{L_l} + \widehat{r}_{22} \frac{q_v^{L_l}}{R T_l^{L_l}} \ . \tag{2.36}$$

vap. vel.	$v_v^{L_l} = -\left(\frac{\rho_v^{L_l}}{\rho_l} - 1\right)\left(\frac{\widehat{r}_{12}k_v}{\widehat{r}_{11}R}\frac{1}{\rho_v^{L_l}T_l^{L_l}}\left[\frac{\partial T_v}{\partial x}\right]_{L_l} + \frac{1}{\widehat{r}_{11}\rho_v^{L_l}}\frac{p_{sat}^{L_l} - R\rho_v^{L_l}T_v^{L_l}}{\sqrt{2\pi R T_l^{L_l}}}\right)$
vap. pr.	$p_v(H,t) = p_{bv} = const.$
liqu. pr.	$p_l = p_v$
liq. tem.	$T_l(0,t) = T_{bl} = const.$
liq. tem.	$\left[\frac{\partial T_l}{\partial x}\right]_{L_l} = -\frac{1}{k_l}\left(\begin{array}{c}\left(c_v^p\left(T_v - T_0\right) + h_{gl}^0\right)\rho_v^{L_l}v_v^{L_l} - k_v\left[\frac{\partial T_v}{\partial x}\right]_{L_l} \\ + \left(\left(-c_v^pT_v + c_v^pT_0 - h_{gl}^0\right)\rho_v^{L_l} + \rho_l c_l\left(T_l - T_0\right)\right)\left(\frac{\rho_v^{L_l}v_v^{L_l}}{\rho_v^{L_l} - \rho_l}\right)\end{array}\right)$
vap. tem.	$T_v(H,t) = T_{bv} = const.$
vap. tem.	$\left[\frac{\partial T_v}{\partial x}\right]_{L_l} = \frac{R}{\widehat{r}_{22}k_v}T_l^{L_l}\left(\widehat{r}_{21}\rho_v^{L_l}\left(v_v^{L_l} - \frac{\rho_v^{L_l}v_v^{L_l}}{\rho_v^{L_l} - \rho_l}\right) + \frac{p_{sat}^{L_l}}{\sqrt{2\pi R T_l}}\frac{\left(T_v^{L_l} - T_l^{L_l}\right)}{T_l^{L_l}}\right)$
surf. vel.	$\frac{dL_l}{dt} = \frac{\rho_v^{L_l}v_v^{L_l}}{\rho_v^{L_l} - \rho_l}$

Table 2.5: Evaporation interface and boundary conditions for non-steady system.

The Onsager coefficients, which describe the linear relation between thermodynamic fluxes and forces can be taken from (D.2) or (D.3) in Appendix D. Eq. (2.35) is manipulated by using $j^{L_l} = \rho_v^{L_l}\widehat{v}_v^{L_l}$ or $j^{L_l} = \rho_v^{L_l}\left(v_v^{L_l} - \frac{dL_l}{dt}\right)$ for mass flow and with the ideal gas law and Eq. (1.13) and (2.30) it follows

$$v_v^{L_l} = -\left(\frac{\rho_v^{L_l}}{\rho_l} - 1\right)\left(\frac{\widehat{r}_{12}k_v}{\widehat{r}_{11}R}\frac{1}{\rho_v^{L_l}T_l^{L_l}}\frac{\partial T_v^{L_l}}{\partial x} + \frac{1}{\widehat{r}_{11}\rho_v^{L_l}}\frac{p_{sat}^{L_l} - R\rho_v^{L_l}T_v^{L_l}}{\sqrt{2\pi R T_l^{L_l}}}\right) . \tag{2.37}$$

Eq. (2.36) is manipulated in the same manner and then reads

$$\frac{\partial T_v^{L_l}}{\partial x} = \frac{R}{\widehat{r}_{22}k_v}T_l^{L_l}\left(\widehat{r}_{21}\rho_v^{L_l}\left(v_v^{L_l} - \frac{\rho_v^{L_l}v_v^{L_l}}{\rho_v^{L_l} - \rho_l}\right) + \frac{p_{sat}^{L_l}}{\sqrt{2\pi R T_l}}\frac{\left(T_v^{L_l} - T_l^{L_l}\right)}{T_l^{L_l}}\right) . \tag{2.38}$$

Table 2.5 summarizes all interface and boundary conditions for the one-dimensional and non-steady system.

vap. vel.	$\overline{v}_v^{L_l} = \frac{1}{v_0}\left(1 - \frac{p_0}{RT_0\rho_l}\right)\begin{pmatrix} \frac{\widehat{r}_{12}k_vT_0}{\widehat{r}_{11}p_0L}\left[\frac{\partial\overline{T}_v}{\partial\overline{x}}\right]_{L_l} + \\ \frac{1}{\widehat{r}_{11}p_0\sqrt{2\pi RT_0}}\left(p_0h_{gl}^0\overline{T}_l^{L_l} - RT_0p_0\overline{p}_v^{L_l}\right) \end{pmatrix}$
vap. pr.	$\overline{p}_{bv} = \frac{p_{bv}}{p_0} - 1$
liqu. pr.	$\overline{p_l} = \overline{p_v}$
liq. tem.	$\overline{T}_{bl} = \frac{T_{bl}}{T_o} - 1$
liq. tem.	$\left[\frac{\partial\overline{T}_l}{\partial\overline{x}}\right]_{L_l} = \frac{1}{k_l}\left(\frac{L\rho_{v0}h_{gl}^0v_0}{T_o}\overline{v}_v^{L_l}\left(\frac{\rho_l}{\rho_{vo}-\rho_l}\right) + k_v\left[\frac{\partial\overline{T}_v}{\partial\overline{x}}\right]_{L_l}\right)$
vap. tem.	$\overline{T}_{bv} = \frac{T_{bv}}{T_o} - 1$
vap. tem.	$\left[\frac{\partial\overline{T}_v}{\partial\overline{x}}\right]_{L_l} = \frac{LR}{\widehat{r}_{22}k_v}\left(\widehat{r}_{21}\rho_{v0}\left(-\frac{\rho_l}{\rho_{v0}-\rho_l}\right)v_0\overline{v}_v^{L_l} + \frac{p_0}{\sqrt{2\pi RT_0}}\left(\overline{T}_v - \overline{T}_l\right)\right)$
surf. vel.	$\frac{d\overline{L_l}}{d\bar{t}} = \frac{\rho_{v0}\overline{v}_v^{L_l}}{\rho_{v0}-\rho_l}$

Table 2.6: Linearized and non-dimensional interface and boundary conditions for non-steady system.

2.3.1 Linearizing and non-dimensionalizing the boundary conditions

The interface and boundary conditions, Table 2.5 shall be linearized and non-dimensionalized in the same way as the Navier-Stokes-Fourier equations by using (2.15). The saturation pressure is approximated with the Clausius-Clapeyron equation which in linear and non-dimensional form (variables denote deviation to equilibrium) can be written as $\overline{p_{sat}}\left(T^l\right) = \frac{h_{gl}^0}{RT_0}\overline{T^l}$. The linear and non-dimensional boundary conditions are summarized in Table 2.6

2.3.2 Analytical steady-state solution

A full set of equations to describe Fig. 2.1 is obtained from the simplified Navier-Stokes-Fourier equations in Table 2.4 together with the initial- and boundary conditions given in Tables 2.2 and 2.6. For gaining a steady-state solution, one considers the interface between liquid and vapor to be fixed, i.e., $\frac{dL_l}{dt} = 0$. With all time derivatives being zero, the temperature profiles which follow after integration of Eq. (2.23) and (2.25) are linear and the solution of the vapor velocity implicitly given by (2.21) is constant. As comparison to the non-steady solution, a steady-state solution shall be obtained by solving the two modified Onsager boundary conditions (2.37,2.38) together with the integrated energy balance (2.34) and the controlled boundary temperatures as a linear system. The solution must satisfy

$$\overline{T_l} = (A_l + B_l x) \quad , \tag{2.39}$$

$$\overline{T_v} = (A_v + B_v x) \ , \tag{2.40}$$

$$\overline{v_v} = C_v = const. \ . \tag{2.41}$$

For the linear system it follows

$$\begin{pmatrix} f_1 \frac{h_{gl}^0}{\widehat{r}_{11}\sqrt{2\pi R T_0}} & 0 & 0 & f_1 \frac{\widehat{r}_{12} k_v T_0}{\widehat{r}_{11} p_0 L} & 1 \\ 0 & 0 & 1 & -\frac{k_v}{k_l} & -\frac{1}{k_l}\frac{L\rho_{v0} h_{gl}^o v_0}{T_0} f_3 \\ f_2 & -f_2 & 0 & 1 & \frac{\widehat{r}_{21}\rho_{v0} L R v_0}{\widehat{r}_{22} k_v} f_3 \\ 1 & 0 & -\frac{L_{l0}}{L} & 0 & 0 \\ 0 & 1 & 0 & \left(\frac{H-L_{l0}}{L}\right) & 0 \end{pmatrix} \begin{pmatrix} A_l \\ A_v \\ B_l \\ B_v \\ C_v \end{pmatrix} = \begin{pmatrix} f_1 \frac{R T_0 \overline{p}_v^{L_l}}{\widehat{r}_{11}\sqrt{2\pi R T_0}} \\ 0 \\ 0 \\ \frac{T_{bl}}{T_0} - 1 \\ \frac{T_{bv}}{T_0} - 1 \end{pmatrix} , \tag{2.42}$$

with the constants:

$$f_1 = -\frac{1}{v_o}\left(1 - \frac{\rho_{v0}}{\rho_l}\right) \ , \tag{2.43}$$

$$f_2 = \frac{LR}{\widehat{r}_{22} k_v} \frac{p_0}{\sqrt{2\pi R T_0}} \ , \tag{2.44}$$

$$f_3 = \frac{\rho_l}{\rho_{v0} - \rho_l} \ . \tag{2.45}$$

2.4 Numerical method

2.4.1 Computational domain and discretization

The simplified NSF equations, Tables 2.4 and 2.6, shall be solved numerically in the following. Due to simple geometry, a uniform mesh, depicted in Fig. 2.2 for both liquid and vapor appears convenient. The height of the system is split into N_l subdivisions

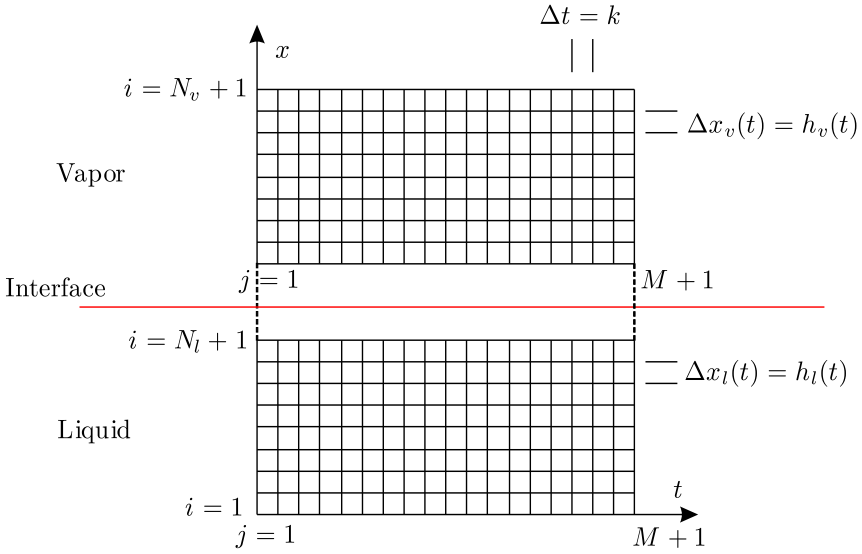

Figure 2.2: Discretized computational domain for non-steady evaporation system.

of size $\Delta x_l(t) = h_l(t)$ for liquid and N_v subdivisions of size $\Delta x_v(t) = h_v(t)$ for vapor with $h_l\,(t=0) = h_v\,(t=0) = h$. The location is given by $i_\alpha = \{1, ..., N_\alpha + 1\}$ for space and $j = \{1, ..., M + 1\}$ for time. The differential equations (2.23) and (2.25) are of the form

$$\frac{\partial \overline{T}}{\partial \overline{t}} - a \frac{\partial^2 \overline{T}}{\partial \overline{x}^2} = 0 \ , \tag{2.46}$$

which after discretization may be written as

$$\left[\frac{\partial \overline{T}}{\partial \overline{t}}\right]_{i,j-1} - a \left[\frac{\partial^2 \overline{T}}{\partial \overline{x}^2}\right]_{i,j-1} = 0 \ . \tag{2.47}$$

An explicit form is obtained by using a forward difference for the time derivative and a central difference for the spatial derivative given as

$$\left[\frac{\partial \overline{T}}{\partial \overline{t}}\right]_{i,j-1} = \frac{\overline{T}_{i,j} - \overline{T}_{i,j-1}}{k} + O\,(k) \ , \tag{2.48}$$

$$\left[\frac{\partial^2 \overline{T}}{\partial \overline{x}^2}\right]_{i,j-1} = \frac{\overline{T}_{i+1,j-1} - 2\overline{T}_{i,j-1} + \overline{T}_{i-1,j-1}}{h^2} + O\left(h_v^2\right) \ . \tag{2.49}$$

By approximating derivatives with finite differences, an error $O(h_v^2)$ is introduced. The explicit solution for the temperature profiles reads

$$\overline{T}_{i,j} = \overline{T}_{i,j-1} + a\frac{k}{h^2}\left(\overline{T}_{i+1,j-1} - 2\overline{T}_{i,j-1} + \overline{T}_{i-1,j-1}\right) \ . \tag{2.50}$$

The velocity may be calculated with Eq. (2.24), which is of the form

$$\frac{\partial v_v}{\partial x} - a\frac{\partial^2 T_v}{\partial x^2} = 0 \ . \tag{2.51}$$

For velocity at $i = 2$, a first order backward and a second order central difference are used which are given as

$$\left(\frac{\partial \overline{v}_v}{\partial x}\right)_{2,j} = \frac{\overline{v}_{v,2,j} - \overline{v}_{v,1,j}}{h_v} + O\left(h_v\right) \ , \tag{2.52}$$

$$\left(\frac{\partial^2 \overline{T}_v}{\partial \overline{x}^2}\right)_{2,j} = \frac{\overline{T}_{v,3,j} - 2\overline{T}_{v,2,j} + \overline{T}_{v,1,j}}{h_v^2} + O\left(h_v^2\right) \ . \tag{2.53}$$

Since a central difference of higher accuracy can not be used for $\left(\frac{\partial v_v}{\partial x}\right)_{2,j}$ at $i = 2$, a backward difference (2.52) is necessary. Then the explicit form for calculating the velocity at $i = 2$ becomes

$$v_{v,2,j} = \frac{v}{h_v}\left(\overline{T}_{v,3,j} - 2\overline{T}_{v,2,j} + \overline{T}_{v,1,j}\right) + v_{v,1,j} \ . \tag{2.54}$$

For velocity at $i = 3...N_v + 1$ two second order central differences are used:

$$\frac{\partial \overline{v}_v}{\partial \overline{x}} = \left(\frac{\partial \overline{v}_v}{\partial \overline{x}}\right)_{i-1,j} = \frac{\overline{v}_{v,i,j} - \overline{v}_{v,i-2,j}}{2h_v} + O\left(h_v^2\right) \ , \tag{2.55}$$

$$\left[\frac{\partial^2 \overline{T}_v}{\partial \overline{x}^2}\right]_{i-1,j} = \frac{\overline{T}_{v,i,j} - 2\overline{T}_{v,i-1,j} + \overline{T}_{v,i-2,j}}{h_v^2} + O\left(h_v^2\right) \ . \tag{2.56}$$

The velocity follows as

$$\overline{v}_{v,i,j} = \frac{2}{h_v}\overline{v}\left(\overline{T}_{v,i,j} - 2\overline{T}_{v,i-1,j} + \overline{T}_{v,i-2,j}\right) + \overline{v}_{v,i-2,j} \ . \tag{2.57}$$

$$c_1 = \frac{1}{v_0}\frac{1}{k_l}\frac{L\rho_{vo}h_{gl}^0 v_0}{T_0} \ , \quad c_2 = \frac{\widehat{r}_{12}k_v T_0}{\widehat{r}_{11}p_0 L}, \quad c_3 = \frac{k_v}{k_l} \ , \quad c_4 = RT_0 p_0 \overline{p}_v^{L_l} \ ,$$

$$c_5 = \frac{1}{\widehat{r}_{11}p_0\sqrt{2\pi RT_0}} \ , \quad c_6 = \frac{1}{\left(\frac{1}{LR}k_v\widehat{r}_{22} - \widehat{r}_{21}\rho_{v0}\frac{\widehat{r}_{12}k_v T_0}{\widehat{r}_{11}p_0 L}\right)} \ , \quad c_7 = \frac{\widehat{r}_{21}\rho_{v0}}{\widehat{r}_{11}p_0\sqrt{2\pi RT_0}} \ ,$$

$$c_8 = \frac{p_0}{\sqrt{2\pi RT_0}} \ , \quad c_9 = p_0 h_{gl}^0 \ .$$

Table 2.7: Constants for the solution of linear system

Equations to determine $\overline{T_l}\,(N_l+1)$, $\overline{T_v}\,(1)$ and $\overline{v_v}\,(1)$ are found in the two evaporation Onsager boundary conditions (2.37,2.38) and the integrated energy balance (2.34). One sided differences as below are used for the three equations which form a linear system:

$$\left(\frac{\partial \overline{T_v}}{\partial x}\right)_{1,j} = \frac{-3\overline{T}_{v,1,j} + 4\overline{T}_{v,2,j} - \overline{T}_{v,3,j}}{2h_v} + O\left(h_v^2\right) \ ,$$

$$\left(\frac{\partial \overline{T_l}}{\partial x}\right)_{N_l+1,j} = \frac{\overline{T}_{l,N_l-1,j} - 4\overline{T}_{l,N_l,j} + 3\overline{T}_{l,N_l+1,j}}{2h_l} + O\left(h_l^2\right) \ . \tag{2.58}$$

The first Onsager boundary condition (2.37) is used to eliminate the vapor velocity $\overline{v_v}\,(1)$ in the integrated energy balance (2.34) and in the second Onsager boundary condition (2.38), and the linear system follows as

$$\begin{pmatrix} (3 + 2h_l c_1 c_5 c_9) & -3\,(c_1 c_2 - c_3)\,\frac{h_l}{h_v} \\ -2h_v\,(c_6 c_7 c_9 - c_6 c_8) & (-3 - 2h_v c_6 c_8) \end{pmatrix} \begin{pmatrix} \overline{T}_{l,N_l+1,j} \\ \overline{T}_{v,1,j} \end{pmatrix} =$$
$$\begin{pmatrix} 2h_l c_1 c_5 c_4 - \overline{T}_{l,N_l-1,j} + 4\overline{T}_{l,N_l,j} - (c_1 c_2 - c_3)\,\frac{h_l}{h_v}\left(4\overline{T}_{v,2,j} - \overline{T}_{v,3,j}\right) \\ -2h_v c_6 c_7 c_4 - 4\overline{T}_{v,2,j} + \overline{T}_{v,3,j} \end{pmatrix} \ , \tag{2.59}$$

with the constants $c_1, ..., c_9$ given in Table 2.7. After solving the linear system, the Onsager boundary condition (2.37) can be solved explicitly for the vapor velocity at the boundary $\overline{v_v}\,(1)$. The discretization of the remaining boundary conditions from Table 2.6 is trivial and not further discussed here.

2.4.2 The Matlab algorithm

The non-steady evaporation problem is solved in Matlab for which the algorithm is illustrated as a flow chart in Fig. 2.3. Due to decoupling of the differential equations

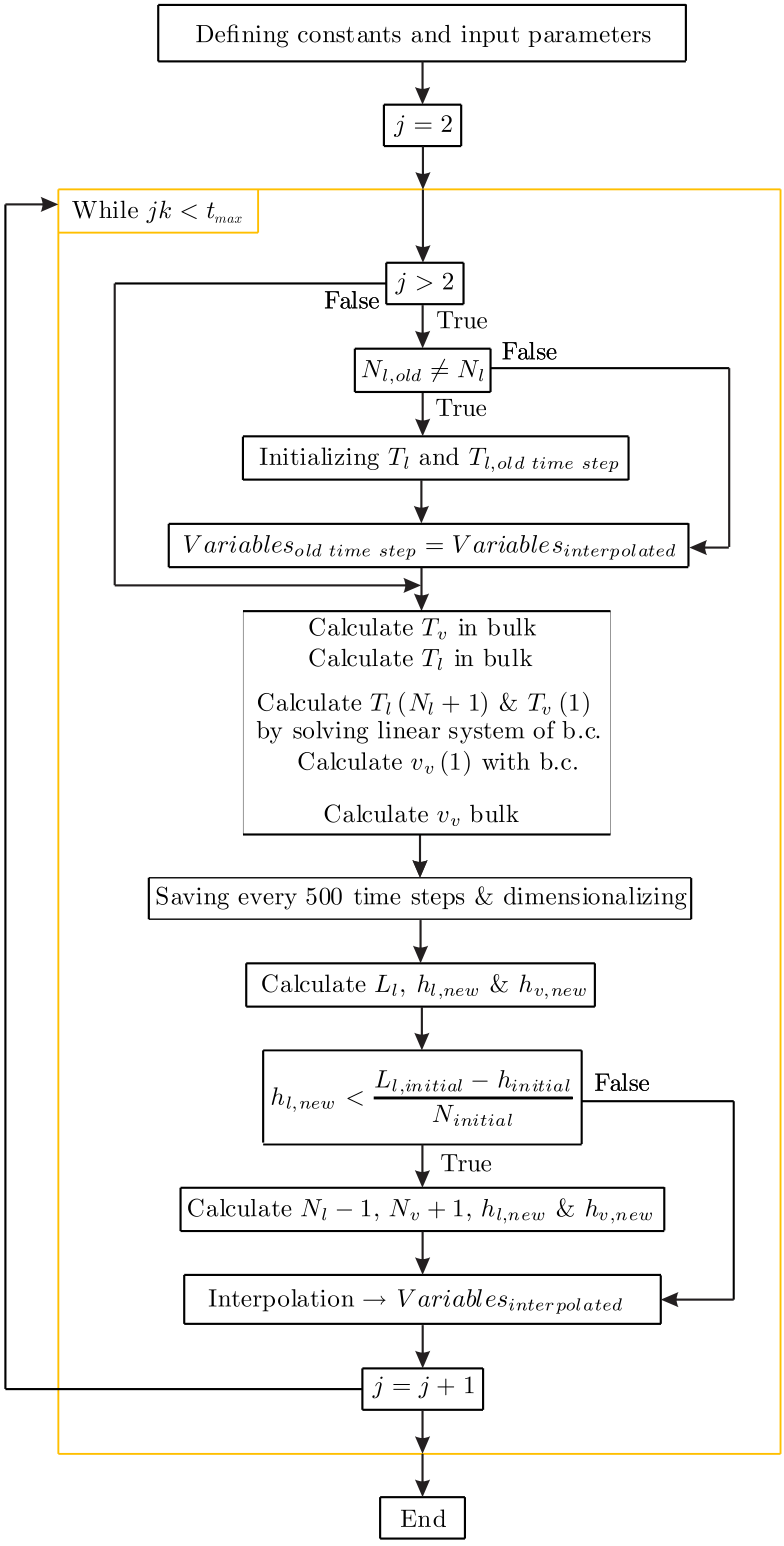

Figure 2.3: Flow chart for numerical solution of non-steady evaporation system.

after simplification, simple explicit solutions can be obtained.

Moving interfaces can be modeled either with dynamic mesh or a level set method, Ref. [19]. Due to simple geometry, a dynamic mesh is chosen here. For every time step j the new position of the interface must be calculated by solving Eq. (2.30). This leads to growing spatial step sizes in vapor h_v and decreasing spatial steps in liquid h_l. This issue suggests to swap nodes after a certain difference between h_v and h_l is reached, i.e., $N_l = N_l - 1$ and $N_v = N_v + 1$. A criterion is suggested in

$$h_{l,new} < h_{critical} = \frac{L_{l,initial} - h_{initial}}{N_{initial}} \ . \tag{2.60}$$

The critical step size of the liquid $h_{critical}$ corresponds to the time, when the interface reaches the next closest node of the initial state, as shown in Figure 2.4.

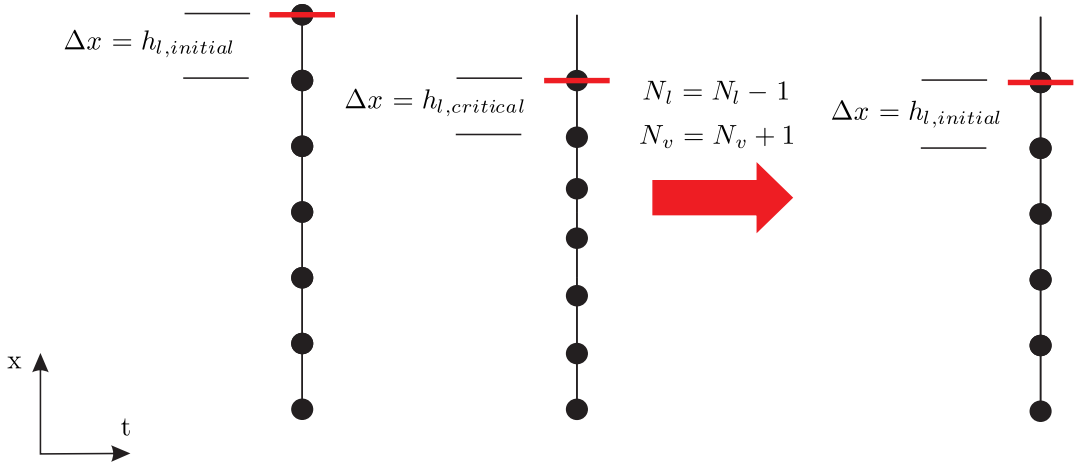

Figure 2.4: Dynamic mesh for non-steady evaporation simulation.

With and without node-swap, all variables are interpolated to the new grid after every time step.

2.5 Results of the non-steady simulation

Explicit numerical methods are restricted to the CFL-criterion, given as

$$a\frac{k}{h^2} < \frac{1}{2} \ , \tag{2.61}$$

with $a = k_v \frac{RT_0}{c_v^p p_0 v_0 L}$ for vapor and $v_0 = \sqrt{RT_0}$. To guarantee a sufficient number of subdivisions for thin fluid layers it is desired to choose the spatial step size h small

Controlled pressure:	$p_v(x = H) = 3000Pa$
Controlled temperatures:	$T_v(x = H) = T_l(x = 0) = 298K$
Evaporation coefficient:	$\vartheta = 0.5$
Onsager coefficients:	$\widehat{r}_{11} = \frac{1}{\vartheta} - 0.40044$
	$\widehat{r}_{12} = 0.126$
	$\widehat{r}_{22} = 0.291$
Initial lengths:	$L_v = L_l = 0.1mm$
Initial spatial subdivisions:	$N_l = N_v = 7$
Number time steps:	$M = 74, 200, 509$
Initial spatial increment:	$h = 1.31 \cdot 10^{-5}mm$
Initial temporal increment:	$k = 5 \cdot 10^{-5}s$
Duration:	$t_{\max} = 10\,\mathrm{sec}$

Table 2.8: Input parameters for non-steady evaporation simulation of thin water layer.

enough. For predicting outcome as far in the future as possible, this effort competes with the need to choose large time steps k. Here, the CFL criterion for the vapor layer is more critical than for the liquid.

2.5.1 Evaporation of water in microscopic system

By using material properties from Table 2.1, slow evaporation of pure water from a thin liquid layer shall be computed. The driving force of the system is pressure on top boundary $p_v(x = H)$ only, given with other input parameters in Table 2.8. The input parameters are chosen in a way to gain a relatively high Knudsen number of $\mathrm{Kn} = \frac{\mu\sqrt{RT}}{pL} = 0.01$. The Onsager coefficients for the interface conditions in Table 2.6 are taken from (D.2). For staying in the linearized regime, a small pressure difference of $169Pa$ between $p_v(x = H)$ and $p_0 = p_{sat}\,(298K) = 3169Pa$ is chosen. Initially, the liquid and vapor layers are equal with $L_v = L_l = 0.1mm$. Even though the Knudsen number is still in a very moderate range, the CFL criterion makes it difficult to gain enough spatial subdivisions while minimizing the temporal subdivisions ($M = 74, 200, 509$ for 10 seconds). The output of the simulation is summarized in Table 2.9.

The liquid layer shrinks in $10sec$ by only $0.023mm$. The liquid temperature at the interface $T_l = 297.1244K$ is slightly larger than for vapor with $T_v = 297.1146K$, though for a significant temperature jump, a Knudsen number of 0.01 appears to be too small. One node is swaped during the simulation. The temperature profiles for liquid and vapor for different times are depicted in Figure 2.5 and compared to

Liquid height:	$L_l\,(t = 10\,\text{sec}) = 0.077mm$
Temperatures:	$T_l\,(x = L_l, t = 10\,\text{sec}) = 297.1244K$
	$T_v\,(x = L_l, t = 10\,\text{sec}) = 297.1146K$
Spatial subdivisions:	$N_v = 8$
	$N_l = 6$
Computational time:	$t_{compute} \approx 8.5\,\text{min}$

Table 2.9: Output parameters for non-steady evaporation simulation of thin water layer.

the analytical steady-state solution, Eq. (2.42). Note that the steady-state solution

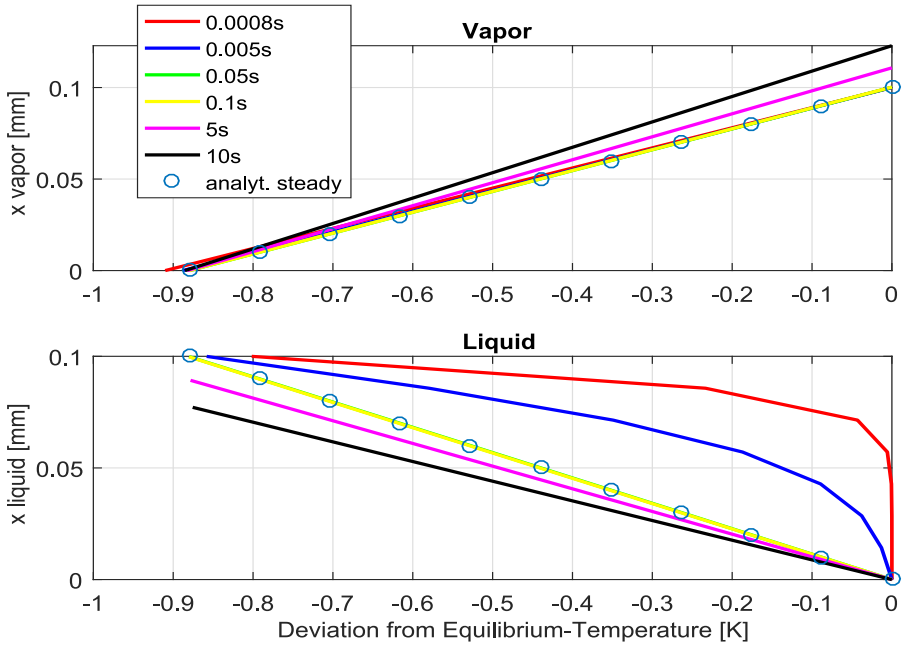

Figure 2.5: Temperature profiles in liquid and vapor for non-steady simulation.

(circles) is obtained for a fixed interface and $L_v = L_l = 0.1mm$, which corresponds to $t = 0s$. In the liquid layer, steady state is reached between $0.005s$ and $0.05s$ after pressure deviation from equilibrium at the top boundary was initiated. In the vapor layer steady state is reached even faster. Since the interface has not moved very far after this short time, the agreement between steady and non-steady solution is excellent for $0.05s$ (green line) and $0.1s$ (yellow line).

Figure 2.6 gives an overview about thermodynamic quantities. One notes the negative conductive heat flux in the vapor which suggests conductive heat transport opposite directed to the fluid flow. This means that part of the required energy for

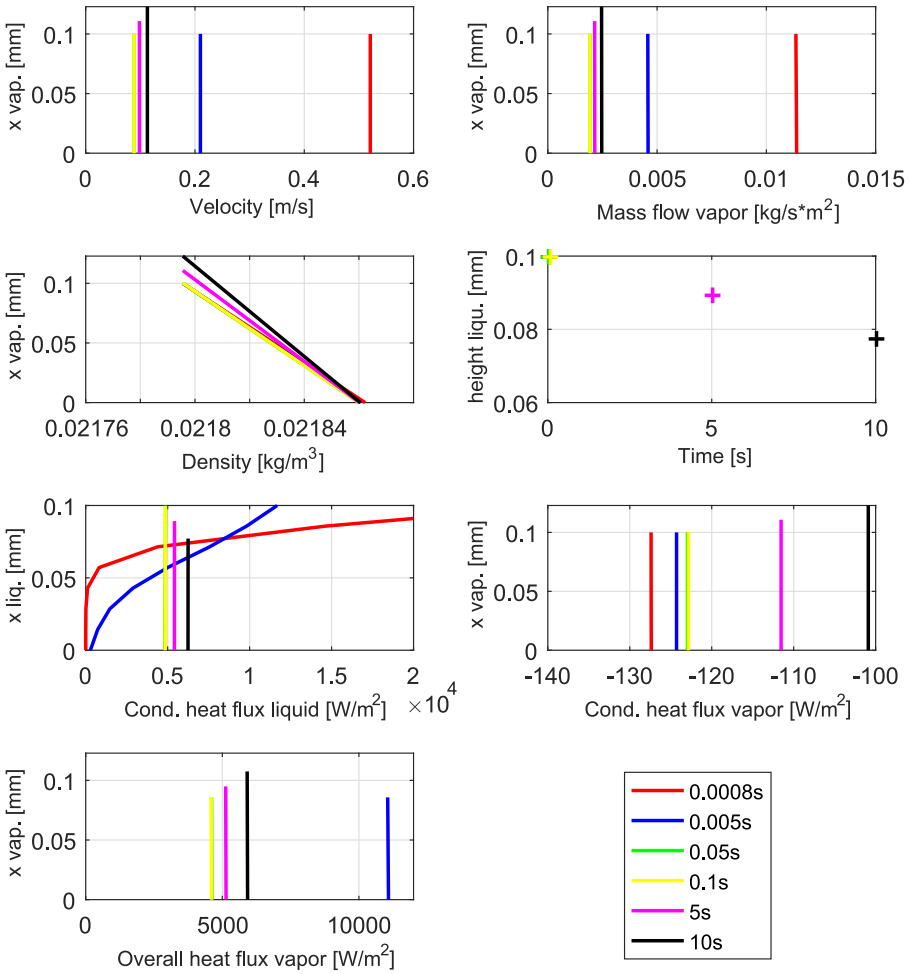

Figure 2.6: Thermodynamic quantities for non-steady evaporation system.

evaporation, the vaporization enthalpy, comes from the top boundary. Though due to the convective heat flux which is dominant here, the overall heat transport in the vapor is positive as expected. The observation of the moving interface allows to calculate the interface velocity, which is nearly constant, see Figure 2.7. The average interface velocity within 10 seconds is $0.0023\frac{mm}{sec}$.

For conducting simulations in the transition regime, the CFL criterion appears to be an issue. Fot future efforts it might be desirable to use an analytic solution or implicit numerical method which is not bound to the CFL restriction.

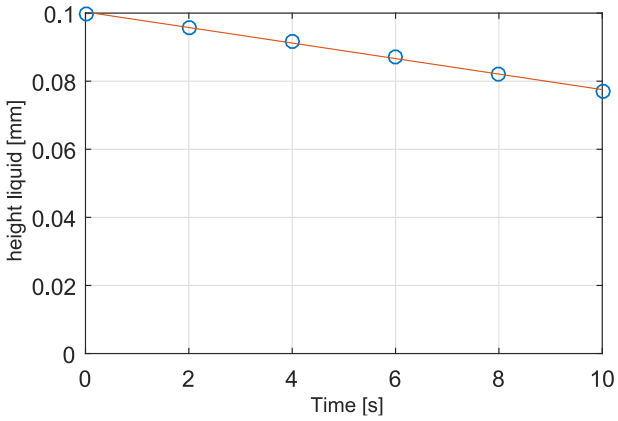

Figure 2.7: Linear approximation to liquid depletion: lines (numerical results), circles (linear approximation).

Chapter 3

Derivation of Evaporation Boundary Conditions for the Linear R13-Equations Based on the Onsager Theory

By combining the Grad and Chapman-Enskog methods into the order of magnitude method, Struchtrup and Torrilhon derived the regularized R13 equations, macroscopic transport equations which account for effects in the transition regime [11][20]. Like all macroscopic transport equations, the R13 equations are an approximation of the Boltzmann equation. R13 introduces higher moments which have a large influence in the rarefied gas regime and small influence in the regime of small Knudsen numbers. Coefficients within the R13 equations allow quick adjustion between different collision models, such as Maxwell molecules, hardspheres or the Bhatnager-Gross-Krook (BGK) model [11]. In the following, only Maxwell molecules will be considered.

Based on microscopic evaporation boundary conditions of the Boltzmann equation, Struchtrup et al. derived macroscopic evaporation boundary conditions for R13 [18]. These equations which are referred to as MBC (Macroscopic Boundary Conditions) in the following show promising results for Knudsen numbers in the transition regime. Here we seek to derive improved evaporation boundary conditions by using an entropy balance integrated around an interface between liquid and vapor phase. Based on the Onsager theory, the integrated entropy balance is rewritten as sum of thermodynamic fluxes and forces [21]. The Onsager theory assumes linear relations

between fluxes and forces and allows one to break the entropy balance into sets of equations, which we utilize as evaporation/condensation boundary condtions [22][23].

A challenge lies in determining the Onsager coefficients, which provide the linear relations between fluxes and forces. The linear R13 equations, accompanied by the new phenomenological boundary conditions (PBC), are solved for two one-dimensional steady-state systems. The first system consists of a vapor phase in between two liquid reservoirs. A DSMC solution for this system is used to fit the Onsager coefficients and to compare the results with the MBC for R13 and also with two Navier-Stokes-Fourier models, which use the Onsager theory as well. The second system is a half space problem [24], for which dimensionless numbers are used to compare the different models.

The remainder of the Chapter proceeds as follows: Sec. 3.1 gives an overview about the R13 equations and the corresponding macroscopic evaporation boundary conditions based on kinetic theory. Sec. 3.2 explains the derivation of the Onsager boundary conditions. Sec. 3.3 shows how the Onsager coefficients are determined, mainly by fitting to DSMC data. The work is discussed in Sec. 3.3.5, Sec. 3.3.6 and in the conclusion, Chap. 5.

3.1 The R13 equations

All equations shall be non-dimensionalized and linearized around an equilibrium state, defined by a reference density for vapor ρ_0 and reference temperature T_0. The equilibrium pressure for both liquid and vapor is defined as $p_0 = p_{sat}(T_0)$. We shall consider small deviations from equilibrium, caused by pressure or temperature gradients, to drive evaporation or condensation. Non-dimensionalizing allows to introduce meaningful coefficients into the equations, e.g., Prandtl or Knudsen numbers. The relations (2.15) which show the connection between variables denoting non-dimensional deviation from an equilibrium state (with overbar) and regular variables, are extended by

$$q_k = \rho_0 \sqrt{RT_o}^3 \overline{q}_k, \qquad \sigma_{ik} = \rho_0 R T_0 \overline{\sigma}_{ik}, \tag{3.1}$$

$$h = h_0 \left(1 + \overline{h}\right), \qquad \eta = \rho s = \eta_0 \left(1 + \overline{\eta}\right),$$

$$v_k = \sqrt{RT_0}\overline{v}_k, \qquad t = \frac{L}{\sqrt{RT_0}}\bar{t}\ .$$

Here, $\eta = \rho s$ is the entropy density and the reference velocity in (2.15) was set to $v_0 = \sqrt{RT_0}$. If not otherwise stated, all following equations use variables denoting deviation from equilibrium, the overbars are neglected. The conservation laws for mass, momentum and energy (1.10-1.12) are given in linearized and dimensionless form as

$$\frac{\partial \rho}{\partial t} + \frac{\partial v_k}{\partial x_k} = 0 \ , \tag{3.2}$$

$$\frac{\partial v_i}{\partial t} + \frac{\partial \sigma_{ik}}{\partial x_k} + \frac{\partial p}{\partial x_i} = g_i \ , \tag{3.3}$$

$$\frac{3}{2}\frac{\partial T}{\partial t} + \frac{\partial v_k}{\partial x_k} + \frac{\partial q_k}{\partial x_k} = 0 \ . \tag{3.4}$$

The ideal gas law $p = \rho RT$ assumes for the non-dimensional and linear case the form $p = \rho + T$, with all variables describing the deviation from the equilibrium state. Equations for heat flux vector q_k and stress tensor σ_{ik} become full balance equations beyond the hydrodynamic regime. By means of the order of magnitude method, Struchtrup & Torrilhon derived the following (here linearized & non-dimensionalized) balance equations from the Boltzmann equation, Ref. [20]:

$$\frac{\partial \sigma_{ij}}{\partial t} + \frac{4}{5}\Pr\frac{\overline{w}_3}{\overline{w}_2}\frac{\partial q_{\langle i}}{\partial x_{j\rangle}} + \frac{\partial m_{ijk}}{\partial x_k} = -\frac{2}{\overline{w}_2}\frac{1}{Kn}\left[\sigma_{ij} + 2Kn\frac{\partial v_{\langle i}}{\partial x_{j\rangle}}\right] \ , \tag{3.5}$$

$$\frac{\partial q_i}{\partial t} + \frac{5}{4\Pr}\frac{\theta_4}{\theta_2}\frac{\partial \sigma_{ik}}{\partial x_k} + \frac{1}{2}\frac{\partial R_{ik}}{\partial x_k} + \frac{1}{6}\frac{\partial \Delta}{\partial x_i} = -\frac{1}{\theta_2}\frac{5}{2\Pr}\frac{1}{Kn}\left[q_i + \frac{5}{2\Pr}Kn\frac{\partial T}{\partial x_i}\right] \ . \tag{3.6}$$

The higher moments are defined over the relations [20]

$$\Delta = -\frac{8Kn}{\Pr_\Delta}\frac{\partial q_k}{\partial x_k} \ , \tag{3.7}$$

$$R_{ij} = -\frac{28}{5}\frac{Kn}{\Pr_R}\frac{\partial q_{\langle i}}{\partial x_{j\rangle}} \ , \tag{3.8}$$

$$m_{ijk} = -\frac{3Kn}{\Pr_M}\frac{\partial \sigma_{\langle ij}}{\partial x_{x\rangle}} \ . \tag{3.9}$$

By using the Chapman-Enskog expansion while considering low Knudsen numbers, Eqs. (3.5, 3.6) reduce to the laws of Navier-Stokes and Fourier, i.e., the left hand sides become zero [11]. The balance laws (3.5,3.6) use the higher moments Δ, R_{ik} and m_{ijk}. Here, $\Pr = \frac{\mu c_p}{k}$ denotes the Prandtl number, with μ as dynamic viscosity, c_p as isobaric specific heat and $k = \frac{15}{4}\mu$ as thermal conductivity. The Knudsen number

	ϖ_2	$\varpi_3 = \theta_4$	θ_2	Pr	$\mathrm{Pr_R}$	$\mathrm{Pr_M}$	Pr_Δ
MM	2	3	45/8	2/3	7/6	3/2	2/3
BGK	2	2	5/2	1	1	1	1
HS	2.02774	2.42113	5.81945	0.6609	1.3307	1.3951	0.9025

Table 3.1: Coefficients for Maxwell (MM), Hard Sphere (HS) and Bhatnager-Gross-Krook (BGK) models for stress tensor and heat flux vector.

is $\mathrm{Kn} = \frac{\mu\sqrt{RT}}{pL}$, with L as characteristic length, e.g., diameter. Here, θ_2, θ_4, $\overline{w}_2$ and $\overline{w}_3$ are coefficients which account for different collision models, such as Maxwell, hard-sphere and BGK models. In the following sections only Maxwell molecules are used. The corresponding coefficients for Maxwell, Hard Sphere or BGK models for stress tensor, heat flux vector and higher moments can be found in Table 3.1 [21].

3.1.1 Macroscopic evaporation boundary conditions for Maxwell molecules

Based on microscopic evaporation boundary conditions of the Boltzmann equation, Struchtrup et al. derived macroscopic evaporation boundary conditions (MBC) for the R13 equations [18]. In these, interface effects are described through the evaporation coefficient ϑ and the accommodation coefficient χ. The evaporation coefficient equals the condensation coefficient, which is the probability that a vapor particle hitting the liquid interface will condense [25].

For the case that a vapor molecule hitting the liquid interface is reflected back to the vapor and not being absorbed, Maxwell proposed an accommodation model which is based on the assumption that the fraction χ of the vapor molecules hitting the liquid surface are diffusively reflected, i.e., with momentum and energy exchange, and the remaining fraction $(1-\chi)$ is specularly reflected, without energy exchange [14]. After non-dimensionalization and linearization around an equilibrium state, the MBC for evaporation [18] assume the form

$$V_n = \sqrt{\frac{2}{\pi}}\frac{\vartheta}{2-\vartheta}\left(p_{sat}\left(T^l\right) - p^g + \frac{1}{2}\left(T^g - T^l\right) - \frac{1}{2}\sigma^g_{nn} + \frac{1}{120}\Delta + \frac{1}{28}R_{nn}\right) \ , \quad (3.10)$$

$$q^g_n = -\sqrt{\frac{2}{\pi}}\frac{\vartheta + \chi(1-\vartheta)}{2-\vartheta-\chi(1-\vartheta)}\left(2\left(T^g - T^l\right) + \frac{1}{2}\sigma^g_{nn} + \frac{1}{15}\Delta + \frac{5}{28}R_{nn}\right) - \frac{1}{2}V^g_n \ , \quad (3.11)$$

$$m_{nnn} = \sqrt{\frac{2}{\pi}} \frac{\vartheta + \chi(1-\vartheta)}{2 - \vartheta - \chi(1-\vartheta)} \left(\frac{2}{5} \left(T^g - T^l \right) - \frac{7}{5} \sigma^g_{nn} + \frac{1}{75} \Delta - \frac{1}{14} R_{nn} \right) - \frac{2}{5} V^g_n \ , \tag{3.12}$$

$$\overline{\sigma}_{nk} = -\sqrt{\frac{2}{\pi}} \frac{\vartheta + \chi(1-\vartheta)}{2 - \vartheta - \chi(1-\vartheta)} \left(\overline{V}^g_{\ k} + \frac{1}{5} \overline{q}^g_k + \frac{1}{2} \overline{m}_{nnk} \right) \ , \tag{3.13}$$

$$\overline{R}_{nk} = \sqrt{\frac{2}{\pi}} \frac{\vartheta + \chi(1-\vartheta)}{2 - \vartheta - \chi(1-\vartheta)} \left(\overline{V}^g_k - \frac{11}{5} \overline{q}^g_k - \frac{1}{2} \overline{m}_{nnk} \right) \ , \tag{3.14}$$

$$\widetilde{m}_{nij} = -\sqrt{\frac{2}{\pi}} \frac{\vartheta + \chi(1-\vartheta)}{2 - \vartheta - \chi(1-\vartheta)} \left(\widetilde{\sigma}^g_{ij} + \frac{1}{14} \widetilde{R}_{ij} + \left(\frac{1}{5} \left(T^g - T^l \right) - \frac{1}{5} \sigma^g_{nn} + \frac{1}{150} \Delta \right) \delta_{ij} \right) + \frac{1}{5} \delta_{ij} V^g_n \ . \tag{3.15}$$

Here, the index n refers to the direction normal to the interface. The variables are tensor components where the overbar denotes the normal-tangential- and tilde the tangential-tangential parts, see Appendix B. Note that all variables describe the deviation from an equilibrium state.

3.2 Deriving the evaporation boundary conditions

We aim to derive phenomenological boundary conditions (PBC) for the regularized R13 equations for a liquid-gas interface. The approach follows Ref. [21] in which a reduced entropy balance is used to derive boundary conditions for a wall-gas interface. The entropy balance for a fluid with dimensionless entropy density $\widetilde{\eta}$, entropy flux Ψ_k and entropy generation rate Σ_{gen} reads

$$\frac{\partial \widetilde{\eta}}{\partial t} + \frac{\partial \Psi_k}{\partial x_k} = \Sigma_{gen} \ . \tag{3.16}$$

Eq. (3.16) shall be integrated over a small volume of area ΔA and height Δx across the liquid-vapor interface. By using Gauss' Theorem, the integrated entropy balance becomes

$$\int\limits_{\Delta A \Delta x} \frac{\partial \widetilde{\eta}}{\partial t} dV + \oint\limits_{\partial \Delta V} \Psi_k n_k dA = \int\limits_{\Delta A \Delta x} \Sigma_{gen} dV \ . \tag{3.17}$$

For $\Delta x \to 0$ the first term vanishes and (3.17) reduces to the entropy balance for the interface,

$$\left(\Psi_k^g - \Psi_k^l\right) n_k = \Sigma_{surface} \ . \tag{3.18}$$

Hence, the entropy generation rate $\Sigma_{surface} = \frac{\int_{\Delta A \Delta x} \Sigma_{gen} dV}{dA}$ is equal to the difference in the entropy fluxes entering and leaving the interface. In the following, all variables on liquid side are indicated with superscript l and all variables on vapor side with g. A linear combination of manipulated mass, energy and entropy balances (Appendix A) leads to the (linearized and non-dimensional) entropy flux on the liquid side as

$$\Psi_k^l = -q_k^l T^l - \sigma_{ik}^l v_i^l - p^l v_k^l \ . \tag{3.19}$$

Here T, ρ and v are deviations to an equilibrium state defined by T_0, ρ_0 and $p_0 = p_{sat}\left(T_0\right)$. For the linear R13 equations and the vapor side, the linearized and dimensionless entropy flux (Appendix A) is

$$\Psi_k^g = -\left(\rho^g + T^g\right) v_k^g - v_i^g \sigma_{ik}^g - T^g q_k^g - \frac{\varpi_3}{5} \Pr q_i^g \sigma_{ik}^g - \frac{\varpi_2}{4} \sigma_{ij}^g m_{ijk} - \frac{2\theta_2}{25} \left(\Pr\right)^2 \left(q_i^g R_{ik} + \frac{\Delta}{3} q_k^g\right) \ . \tag{3.20}$$

Furthermore the (linearized and non-dimensional) balance laws for mass, momentum and energy integrated around the interface similar to (3.18) become

$$\rho_l v_k^l n_k = \rho_0 v_k^g n_k \ , \tag{3.21}$$

$$p^l n_i + \sigma_{ik}^l n_k = p^g n_i + \sigma_{ik}^g n_k \ , \tag{3.22}$$

$$\frac{\rho_l h_0^l}{R \rho_0 T_0} v_k^l n_k + q_k^l n_k = \frac{h_o^g}{R T_o} v_k^g n_k + q_k^g n_k \ . \tag{3.23}$$

The variables v_k^l and v_k^g are the velocities on liquid and on vapor side at the interface, from the perspective of an observer resting on the interface. The entropy fluxes (3.19,3.20) are plugged into the integrated entropy balance (3.18). Eqs. (3.21-3.23) are used to eliminate most variables on liquid side. All variables describe the deviation from equilibrium, are dimensionless and linearized. After applying the appropriate coefficients for Maxwell molecules, according to Table 3.1, using the Clausius Clapeyron equation [2] (linearized and dimensionless) in the form $p_{sat}\left(T^l\right) = \frac{h_{gl}^0}{R T_0} T^l$ and by

considering $\rho_l \gg \rho_0$ one may write (3.18) as below

$$J_k^g n_k \frac{1}{\rho_0}\left(p_{sat}\left(T^l\right)-p^g\right)-\left(T^g-T^l\right)q_k^g n_k - V_i\sigma_{ik}^g n_k - \frac{\varpi_3}{5}\Pr q_i^g\sigma_{ik}^g n_k \\ -\frac{\varpi_2}{4}\sigma_{ij}^g m_{ijk}n_k - \frac{2\theta_2}{25}(\Pr)^2\left(q_i^g R_{ik}n_k+\frac{\Delta}{3}q_k^g n_k\right)=\Sigma_{surface}\ . \quad (3.24)$$

where $V_i = v_i^g - v_i^l$, $J_k^g n_k = \rho_0 v_k^g n_k$ and the corresponding ideal gas law, given as $\rho^g = p^g - T^g$ was used. To accomplish a proper entropy balance for the linearized equations, terms up to second order are kept.

Next, the entropy balance is split into normal and tangential components. All matrices and higher moments are symmetric and trace free:

$$\begin{aligned}\Sigma_{surface} = {} & J_n^g\frac{1}{\rho_0}\left[p_{sat}\left(T^l\right)-p^g-\sigma_{nn}\right] \\ & + q_n^g\left[-\left(T^g-T^l\right)-\frac{\varpi_3}{5}\Pr\sigma_{nn}-\frac{2\theta_2}{25}(\Pr)^2\left(R_{nn}+\frac{\Delta}{3}\right)\right] \\ & + m_{nnn}\left[-\frac{3\varpi_2}{8}\sigma_{nn}\right] \\ & + \overline{\sigma}_{nk}\left[-\overline{V}_k-\frac{\varpi_3}{5}\Pr\overline{q}_k-\frac{\varpi_2}{2}\overline{m}_{nnk}\right]+\overline{R}_{nk}\left[-\frac{2\theta_2}{25}(\Pr)^2\overline{q}_k\right] \\ & + \widetilde{m}_{nij}\left[-\frac{\varpi_2}{4}\widetilde{\sigma}_{ij}\right] \end{aligned} \quad (3.25)$$

.

As before, overbar denotes normal-tangential- and tilde denotes tangential-tangential components (Appendix B). If the mass flow J_n^g vanishes, Eq. (3.25) simplifies to the entropy generation at a wall-gas-interface, see Ref. [21].

The entropy generation may be written as a superposition of thermodynamic fluxes J_i and forces X_i [22][23]:

$$\sigma = \sum_i J_i X_i \geq 0\ . \quad (3.26)$$

Here, moments with odd degree in the normal direction n are identified as fluxes, i.e., J_n, q_n, m_{nnn}, $\overline{\sigma}_{nk}$, $\overline{R}_{nk}$ and $\widetilde{m}_{nij}$, while moments with even degree in n are identified as the corresponding forces, i.e., p^g, T^g, T^l, σ_{nn}, R_{nn}, Δ, $\overline{V}_k$, $\overline{q}_k$, $\overline{m}_{nnk}$ and $\widetilde{\sigma}_{ij}$. Here, p^g, T^g, T^l, σ_{nn}, R_{nn}, Δ, J_n, q_n and m_{nnn} are scalars, $\overline{V}_k$, $\overline{q}_k$, $\overline{m}_{nnk}$, $\overline{\sigma}_{nk}$ and $\overline{R}_{nk}$ are vectors and $\widetilde{\sigma}_{ij}$ and $\widetilde{m}_{nij}$ are tensors. Furthermore, a linear force-flux relation is

stated within the Onsager theory to satisfy Eq. (3.26):

$$J_i = \sum_j L_{ij} X_j \ , \tag{3.27}$$

where, L_{ij} is a symmetric and positiv-definite matrix of Onsager coefficients with the Onsager reciprocity relation given as $L_{ij} = L_{ji}$. Only equations of the same tensor rank are coupled over the reciprocity relation (Curie principle, [26]). This means that all force terms of the same tensor rank superimpose each other and impact all fluxes of the same tensor rank, hence:

Scalar fluxes:

$$\begin{pmatrix} V_n^g \\ q_n^g \\ m_{nnn} \end{pmatrix} = \begin{pmatrix} \lambda_0 & \lambda_1 & \lambda_2 \\ \lambda_1 & \lambda_3 & \lambda_4 \\ \lambda_2 & \lambda_4 & \lambda_5 \end{pmatrix} \begin{pmatrix} \left[p_{sat}\left(T^l\right) - p^g - \sigma_{nn}\right] \\ \left[-\left(T^g - T^l\right) - \frac{\varpi_3}{5}\,\mathrm{Pr}\,\sigma_{nn} - \frac{2\theta_2}{25}\left(\mathrm{Pr}\right)^2\left(R_{nn} + \frac{\Delta}{3}\right)\right] \\ \left[-\frac{3\varpi_2}{8}\sigma_{nn}\right] \end{pmatrix} , \tag{3.28}$$

Vector fluxes:

$$\begin{pmatrix} \overline{\sigma}_{nk} \\ \overline{R}_{nk} \end{pmatrix} = \begin{pmatrix} \zeta_0 & \zeta_1 \\ \zeta_1 & \zeta_2 \end{pmatrix} \begin{pmatrix} \left[-\overline{V}_k - \frac{\varpi_3}{5}\,\mathrm{Pr}\,\overline{q}_k - \frac{\varpi_2}{2}\overline{m}_{nnk}\right] \\ \left[-\frac{2\theta_2}{25}\left(\mathrm{Pr}\right)^2\overline{q}_k\right] \end{pmatrix} , \tag{3.29}$$

Tensor fluxes:

$$\widetilde{m}_{nij} = -\kappa_0 \frac{\varpi_2}{4} \widetilde{\sigma}_{ij} \ . \tag{3.30}$$

For all $\lambda_{0,\ldots,2} = 0$ one obtains the full set of phenomenological boundary conditions for a wall-gas interface, see Ref. [21]. The interface conditions (3.29-3.30), which consist of first order tensors (vectors) and second order tensors (matrices), respecitvely, have been fitted for a wall-gas interface in Ref. [21]. The fitting of (3.28) for evaporation at liquid-vapor interfaces is discussed in Sec. 3.3. The new evaporation boundary conditions (3.28-3.30) shall be referred to as PBC (Phenomenological Boundary Conditions) in the following.

3.3 Determining the Onsager coefficients

3.3.1 Comparison to previous macroscopic boundary conditions

The structure between PBC and MBC is very similar, with the main difference, being the coefficients. As first step to determine the Onsager coefficients within the PBC at a liquid-gas interface (3.28-3.30), we try to use the coefficients of the MBC in a way that all terms except those where higher order moments, i.e., Δ, R_{ij}, m_{ijk}, occur are consistent with the MBC. This is justified due to the fact, that the MBC predicts effects in the Navier-Stokes regime very well. In the transition regime, however, their application seems to be more limited [18].

Since the higher moments are responsible for approximating rarefaction effects, a difference between PBC and MBC in these terms is desired.

For a liquid-gas interface, the Onsager matrix of those boundary conditions with variables of zero tensor rank (3.28) assumes the dimension 3x3, in contrast to the wall-gas interface ($V_n^g = 0$) where the dimension is 2x2 [21]. It follows that it is not possible to have all terms which consist of p^g, σ_{nn} and $\left(T^g - T^l\right)$ equal between PBC and MBC. Hence, one has a certain degree of freedom to choose which coefficients to use from the MBC. Based on these thoughts, the following Onsager coefficients are suggested:

$$\lambda_0 = a\sqrt{\frac{2}{\pi}}\frac{\vartheta}{2-\vartheta} \ , \tag{3.31}$$

$$\lambda_1 = b\left(-\frac{1}{2}\sqrt{\frac{2}{\pi}}\frac{\vartheta}{2-\vartheta}\right) \ , \tag{3.32}$$

$$\lambda_2 = c\left(-\frac{2}{5}\sqrt{\frac{2}{\pi}}\frac{\vartheta}{2-\vartheta}\right) \ , \tag{3.33}$$

$$\lambda_3 = d\left(2\sqrt{\frac{2}{\pi}}\frac{\vartheta+\chi(1-\vartheta)}{2-\vartheta-\chi(1-\vartheta)}\right) \ , \tag{3.34}$$

$$\lambda_4 = e\left(-\frac{2}{5}\sqrt{\frac{2}{\pi}}\frac{\vartheta+\chi(1-\vartheta)}{2-\vartheta-\chi(1-\vartheta)}\right) \ , \tag{3.35}$$

$$\lambda_5 = f \left(\begin{array}{c} \frac{1}{\varpi_2}\left(\frac{56}{15} + \frac{16}{75}\varpi_3 \,\mathrm{Pr}\right)\sqrt{\frac{2}{\pi}}\frac{\vartheta+\chi(1-\vartheta)}{2-\vartheta-\chi(1-\vartheta)} \\ +\frac{8}{\varpi_2 15}\sqrt{\frac{2}{\pi}}\frac{\vartheta}{2-\vartheta} \end{array} \right) . \tag{3.36}$$

To leave the coefficients adjustable, the factors $a - f$ have been added. Even for $a = b = ... = f = 1$, the PBC differ from the MBC not only in the higher order terms, but also in some lower order terms, see Appendix C. The boundary conditions (3.29-3.30) have been fitted for a wall-gas interface in Ref. [21] and shall not further be investigated here. To determine the coefficients $a, b, ..., f$ by fitting to a DSMC solution, two evaporation problems will be discussed, for which analytical solutions for R13 with PBC can be obtained.

3.3.2 Simplification of R13 for 1-D problems

As can be expected, the present PBC just like the MBC give less accurate results than methods that solve the full Boltzmann equation. The R13 equations and their corresponding boundary conditions are approximations to the Boltzmann equation and carry less information. The adjustable coefficients a-f in (3.31) - (3.36) leave six degress of freedom to determine the Onsager coefficients.

It is of interest if the simplification of R13 to the Boltzmann equation can be partly corrected by adjusting the Onsager coefficients. In this context we simplify the linear R13 equations for one-dimensional and steady systems and solve them for two problems, previously dicussed in [18]. Then, the new solutions are fitted to DSMC data.

In one-dimensional systems, all variables depend only on the location x. For the rest state, the saturation pressure of the liquid interface is set to $p_{sat}(T_0) = p_0$. We assume that the liquid temperature at the interface is controlled. Small pressure or temperature changes are sufficient to drive evaporation or condensation. All equations are linear and dimensionless and describe the deviation from their equilibrium state. The simplified balance equations for mass, momentum and energy read

$$\frac{\partial v}{\partial x} = \frac{\partial \sigma}{\partial x} + \frac{\partial p}{\partial x} = \frac{\partial q}{\partial x} = 0 \; . \tag{3.37}$$

After simple integration follows

$$v = V_0 = const\ , \qquad p + \sigma = P_0 = const\ , \qquad q_0 = Q_0 = const\ . \tag{3.38}$$

Hence, velocity and conductive heat flux are constant in the vapor phase. The normal components of the linear and non-dimensional constitutive equations for (3.7) - (3.9) obtain the form

$$\Delta = -\frac{8Kn}{\mathrm{Pr}_\Delta}\frac{\partial q}{\partial x} = 0\ , \qquad R_{nn} = -\frac{28}{5}\frac{Kn}{\mathrm{Pr}_R}\frac{\partial q}{\partial x} = 0\ , \qquad m_{nnn} = -\frac{3Kn}{\mathrm{Pr}_M}\frac{\partial \sigma}{\partial x}\ , \tag{3.39}$$

with data to adjust between the molecule models from Table 3.1. The linear and non-dimensional equations for normal stress σ and conductive heat flux q_o become

$$\frac{6}{5}Kn\frac{\partial^2\sigma}{\partial x^2} = \frac{\sigma}{Kn}\ , \tag{3.40}$$

$$\frac{\partial\theta}{\partial x} = -\frac{4q_0}{15Kn} - \frac{2}{5}\frac{\partial\sigma}{\partial x}\ . \tag{3.41}$$

Integration yields

$$\sigma = A\sinh\left[\sqrt{\frac{5}{6}}\frac{x}{Kn}\right] + B\cosh\left[\sqrt{\frac{5}{6}}\frac{x}{Kn}\right]\ , \tag{3.42}$$

$$T_g = K - \frac{4q_0x}{15Kn} - \frac{2}{5}\sigma\ . \tag{3.43}$$

with A, B, K as constants of integration. There are 6 unknowns (V_0, P_0, Q_0, A, B, K) that must be determined for finding the solution. For evaporating interfaces, and by taking $\Delta = R = 0$ (3.39) into account, the normal boundary conditions (3.28)-(3.30) simplify to

$$V_{o,n} = \lambda_0\left[-P_0 + p_{sat}\left(T^l\right)\right] + \lambda_1\left[-\left(T_g - T_l\right) - \frac{\varpi_3}{5}\mathrm{Pr}\,\sigma_{nn}\right] - \lambda_2\frac{3\varpi_2}{8}\sigma_{nn}\ , \tag{3.44}$$

$$q_{o,n} = \lambda_1\left[-P_0 + p_{sat}\left(T^l\right)\right] + \lambda_3\left[-\left(T_g - T_l\right) - \frac{\varpi_3}{5}\mathrm{Pr}\,\sigma_{nn}\right] - \lambda_4\frac{3\varpi_2}{8}\sigma_{nn}\ , \tag{3.45}$$

$$\frac{6}{5}Kn\left[\frac{\partial\sigma}{\partial x}\right]_n = \lambda_2\left[P_0 - p_{sat}\left(T^l\right)\right] + \lambda_4\left[\left(T_g - T_l\right) + \frac{\varpi_3}{5}\mathrm{Pr}\,\sigma_{nn}\right] + \lambda_5\frac{3\varpi_2}{8}\sigma_{nn}\ , \tag{3.46}$$

with $V_{o,n} = n_k V_k$ and $q_{o,n} = q_k n_k$.

3.3.3 Problem I: Vapor layer between two liquid reservoirs

In the first problem for fitting the coefficients $a - f$, and also for getting an insight into the Knudsen layers, we consider one-dimensional, steady-state heat- and mass transfer, within a vapor phase, in between two liquid reservoirs, with controlled temperatures of the liquid interfaces, as depicted in Fig. 3.1. The system has been discussed in [18] and shall be outlined only briefly here. The contribution is the solution of the new phenomenological boundary conditions. The interfaces are located

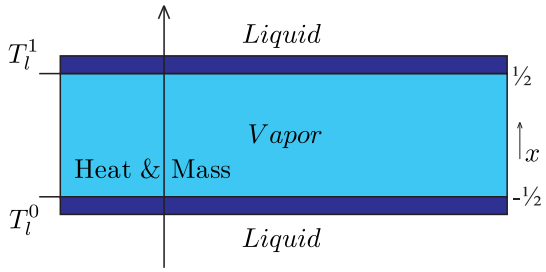

Figure 3.1: System I: Vapor phase between two liquid reservoirs.

at $x = \pm\frac{1}{2}$ with the normal vector n pointing from liquid into vapor and the superscripts 0 for $x = -\frac{1}{2}$ and 1 for $x = \frac{1}{2}$, i.e. $V_{0,n}^0 = -V_{0,n}^1 = V_{0,n}$. Driving force for evaporation and condensation is the temperature difference between T_l^0 and T_l^1. The required six equations are found by evaluating the boundary conditions (3.28) at both interfaces. For evaluation of the equations, it is convenient to take both the sums and the differences at both interfaces. For the three sums follows

$$P_0 = \frac{1}{2}\left(p_{sat}^0(T_l^0) + p_{sat}^0(T_l^1)\right) \ , \tag{3.47}$$

$$\left(T_l^0 + T_l^1\right) - \left(T_g^0 + T_g^1\right) = 0 \ , \tag{3.48}$$

$$\sigma_{nn}^0 = -\sigma_{nn}^1 \ . \tag{3.49}$$

Stress profile, Eq. (3.42) and temperature profile, Eq. (3.43), follow as

$$\sigma = A \sinh\left[\sqrt{\frac{5}{6}}\frac{x}{Kn}\right] \ , \tag{3.50}$$

$$T_g = \frac{(T_l^0 + T_l^1)}{2} - \frac{4q_0 x}{15Kn} - \frac{2}{5}A \sinh\left[\sqrt{\frac{5}{6}}\frac{x}{Kn}\right] \ . \tag{3.51}$$

The three differences of the normal boundary conditions form a linear system for V_0, Q_0 and A as

$$V_0 = \frac{1}{2}\begin{pmatrix} \lambda_0\left[p_{sat}\left(T_l^0\right) - p_{sat}\left(T_l^1\right)\right] \\ +\lambda_1\left[-\frac{4q_0}{15Kn} + \left(T_l^0 - T_l^1\right) + \left(\frac{2\varpi_3}{5}\,\mathrm{Pr} - \frac{4}{5}\right) A\sinh\left[\frac{1}{2}\sqrt{\frac{5}{6}}\frac{1}{Kn}\right]\right] \\ +\frac{3\varpi_2}{4}\lambda_2 A\sinh\left[\frac{1}{2}\sqrt{\frac{5}{6}}\frac{1}{Kn}\right] \end{pmatrix}, \quad (3.52)$$

$$Q_0 = \frac{1}{2}\begin{pmatrix} \lambda_1\left[p_{sat}\left(T_l^0\right) - p_{sat}\left(T_l^1\right)\right] \\ +\lambda_3\left[-\frac{4q_0}{15Kn} + \left(T_l^0 - T_l^1\right) + \left(\frac{2\varpi_3}{5}\,\mathrm{Pr} - \frac{4}{5}\right) A\sinh\left[\frac{1}{2}\sqrt{\frac{5}{6}}\frac{1}{Kn}\right]\right] \\ +\lambda_4\frac{3\varpi_2}{4} A\sinh\left[\frac{1}{2}\sqrt{\frac{5}{6}}\frac{1}{Kn}\right] \end{pmatrix}, \quad (3.53)$$

$$A = \frac{1}{\frac{12}{5}\sqrt{\frac{5}{6}}\cosh(\frac{1}{2}\sqrt{\frac{5}{6}}\frac{1}{Kn})} \begin{pmatrix} \lambda_4\left[\frac{4q_o}{15Kn} + \left(T_l^1 - T_l^0\right) + \left(\frac{4}{5} - \frac{2\varpi_3}{5}\,\mathrm{Pr}\right) A\sinh\left[\frac{1}{2}\sqrt{\frac{5}{6}}\frac{1}{Kn}\right]\right] \\ -\lambda_5\frac{3\varpi_2}{4} A\sinh\left[\frac{1}{2}\sqrt{\frac{5}{6}}\frac{1}{Kn}\right] + \lambda_2\left[p_{sat}\left(T_l^1\right) - p_{sat}\left(T_l^0\right)\right] \end{pmatrix}. \quad (3.54)$$

We refrain from showing the solution but will only show results from the inversion in the figures. For the linear NSF-Onsager boundary conditions, see Appendix D, one finds

$$V_0 = \frac{\widehat{r}_{22}}{\widehat{r}_{11}\widehat{r}_{22} - \widehat{r}_{12}\widehat{r}_{12}}\frac{1}{\sqrt{2\pi}}\frac{1}{2}\begin{pmatrix} p_{sat}^0(T_l^0) - p_{sat}^1(T_l^1) \\ +\frac{\widehat{r}_{12}}{\widehat{r}_{22}}\left(\frac{4Q_0}{15Kn} + T_l^1 - T_l^0\right) \end{pmatrix}, \quad (3.55)$$

$$q_0 = \frac{1}{\widehat{r}_{22}}\frac{1}{2}\left(\frac{1}{\sqrt{2\pi}}\left(-\frac{4Q_0}{15Kn} + T_l^0 - T_l^1\right) - 2\widehat{r}_{12}V_0\right). \quad (3.56)$$

Here A is the amplitude of the Knudsen layer. The given solution for NSF is a simplification for $\chi = \vartheta = 1$, see Appendix D. For the NSF-Onsager coefficients $\widehat{r}_{11}$, $\widehat{r}_{12}$ and $\widehat{r}_{22}$, the Onsager matrix (D.2) or the corrected Onsager matrix (D.3) can be used. The solution of the MBC for this system can be found in [18]. Results shall be compared in Sec. 3.3.5 and 3.3.6.

3.3.4 Problem II: Evaporation in half-space

In the Half Space Problem, a liquid interface evaporates into equilibrium conditions, as discussed previously in Ref. [18]. Driving force is the prescribed pressure p_∞ far

away from the interface, see Fig. 3.2. The six unknowns are found by considering

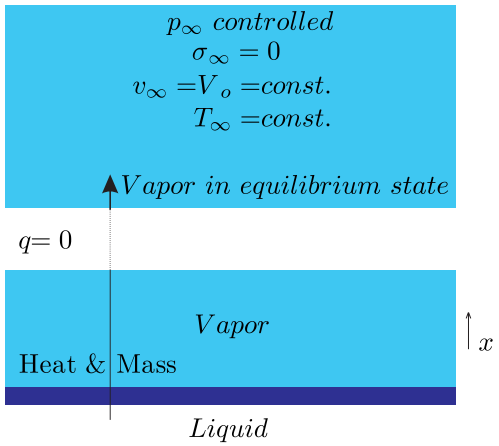

Figure 3.2: System II: Half-space problem.

evaporation boundary conditions on one side and constant velocity $v_\infty = V_0$, pressure $p_\infty = P_0$ and temperature T_∞ far away from the interface. For reaching constant pressure p_∞ and due to the momentum balance (3.38) it is necessary to set the normal stress far away from the interface to $\sigma_\infty = 0$. Moreover conductive heat flux q_0 is set to zero as well. With T_∞ prescribed, one finds the constant K. For (3.50,3.51) it follows

$$\sigma(x) = A \exp\left[-\sqrt{\frac{5}{6}}\frac{x}{Kn}\right] , \tag{3.57}$$

$$T(x) = T_\infty - \frac{2}{5}\sigma(x) . \tag{3.58}$$

Evaluating the boundary conditions (3.28) at the interface between liquid and vapor leads to

$$v_\infty = \lambda_0 \left[p_{sat}(T_l) - p_\infty\right] + \lambda_1 (T_l - T_\infty) + \left(\lambda_1 \left(\frac{2}{5} - \frac{\varpi_3}{5}\,\mathrm{Pr}\right) - \lambda_2 \frac{3\varpi_2}{8}\right) A , \tag{3.59}$$

$$0 = \lambda_1 \left[p_{sat}(T_l) - p_\infty\right] + \lambda_3 (T_l - T_\infty) + \left(\lambda_3 \left(\frac{2}{5} - \frac{\varpi_3}{5}\,\mathrm{Pr}\right) - \lambda_4 \frac{3\varpi_2}{8}\right) A , \tag{3.60}$$

$$0 = \lambda_2 \left[p_{sat}(T_l) - p_\infty\right] + \lambda_4 (T_l - T_\infty) + \left(\lambda_4 \left(\frac{2}{5} - \frac{\varpi_3}{5}\,\mathrm{Pr}\right) - \lambda_5 \frac{3\varpi_2}{8} - \frac{6}{5}\sqrt{\frac{5}{6}}\right) A . \tag{3.61}$$

For Navier-Stokes-Fourier out of Eq. (D.1) follows

$$v_\infty = \frac{p_{sat}(T_l) - p_\infty}{\sqrt{2\pi} r_{11}} \ , \tag{3.62}$$

$$v_\infty = \frac{1}{\sqrt{2\pi}} \frac{T_l - T_\infty}{r_{21}} \ . \tag{3.63}$$

When setting $p_{sat}(T_l) - p_\infty = \Delta p$ and $T_l - T_\infty = \Delta T$, there are four unknowns Δp, ΔT, v_∞ and A, which can be calculated with the PBC (3.59-3.61), if one of the variables is prescribed. For NSF, A is zero and the two equations (3.62, 3.63) are sufficient to be solved as a linear system. The solution for the MBC can again be found in Ref. [18]. Ytrehus, who discussed the half space problem in Ref. [24] proposed dimensionless ratios, in which the pressure difference Δp is eliminated:

$$\alpha_p = \frac{p_{sat}\left(T_l\right) - p_\infty}{\frac{v_\infty}{\sqrt{2}}} \ , \tag{3.64}$$

$$\alpha_\theta = \frac{T_l - T_\infty}{\frac{v_\infty}{\sqrt{2}}} \ . \tag{3.65}$$

This choice allows to gain results, corresponding to pressure and temperature, without prescribing any of the four variables, and it becomes easy to compare different models, such as Maxwell molecules, BGK, Navier-Stokes-Fourier etc. Note that (3.59-3.63) and therefore also (3.64,3.65) are independent of the Knudsen number.

3.3.5 Fitting of the Onsager coefficients: standard temperature profile

The ratios (3.64,3.65) from Problem II together with DSMC data for Problem I shall be used to fit the coefficients a-f. The temperatures and saturation pressures at the liquid boundaries are given as $T_l^0 = p_{sat}(T_l^0) = 1.05$ and $T_l^1 = p_{sat}(T_l^1) = 0.95$. The evaporating material, which is defined over the saturation pressures is artificial. All results in the following are based on full evaporation and fully diffusive reflection, by setting the evaporation and accommodation coefficients to $\vartheta = \chi = 1$. Maxwell molecules are considered and their data is taken out of Table 3.1. In Table 3.2, factors for the Onsager coefficients, used in Eqs. (3.31-3.36), which have been found by trial and error are suggested to adjust the PBC, Eqs. (3.28), for best fit. The results

	a	b	c	d	e	f
PBC standard profile	1.01	0.95	1.30	1.05	0.20	1.10

Table 3.2: Factors to adjust the Onsager coefficients of the PBC for the standard profile.

	α_p	% to Ytrehus	α_θ	% to Ytrehus
PBC standard profile	2.1179	0.35	0.4889	10.33
MBC	2.1097	0.74	0.4894	10.44
NSF	1.9940	6.18	0.4431	-
NSF corrected	2.1254	-	0.4472	0.93
Ytrehus	2.1254	-	0.4431	-

Table 3.3: Solutions for Ytrehus' ratios and percentual deviation to Ytrehus' solution for standard profile.

of the new PBC are compared with the previously derived evaporation boundary conditions (MBC) and also with Navier-Stokes-Fourier. NSF is based on Onsager boundary conditions as well and uses the Onsager matrix (D.2) or the corrected Onsager matrix (D.3). Ytrehus used a moment method to solve the half space problem with high precision [24] and his results are used here as reference. Ytrehus' ratios α_p, α_θ (3.64,3.65) have been calculated for PBC, MBC, NSF and corrected NSF. Together with the percentual deviation to Ytrehus' solution, they are given in Table 3.3. By trial and error fitting of the Onsager coefficients, it was not possible to achieve superior agreement between PBC and DSMC for Problem I (Sec. 3.3.3) and proper results for Ytrehus' ratios (3.64,3.65) at the same time. Forcing good agreement between Ytrehus' solution of the half space problem and PBC regarding the dimensionless ratios showed significant decrease in agreement between PBC and DSMC for Problem I. The fittings that are chosen here are compromises between Problem I and Problem II but with strong emphasis on achieving proper results for Problem I, i.e., proper agreement with DSMC results.

Fig. 3.3 shows temperature and normal stress profiles for Kn = 0.078. R13 with PBC (solid, purple) and MBC (solid, red) are in good agreement with DSMC (green, dashed). The amplitude of the Knudsen layer A is zero for NSF (black, dashed) and corrected NSF (blue, dashed). As a result both NSF solutions slightly deviate from DSMC close to the boundaries. $A = 0$ removes the last term in (3.51) and therefore leads to a linear function. For Problem I, NSF is not able to predict normal stress at all, see Eqs. (3.55, 3.56).

In Fig. 3.4 temperature and normal stress profiles are illustrated for Kn = 0.235.

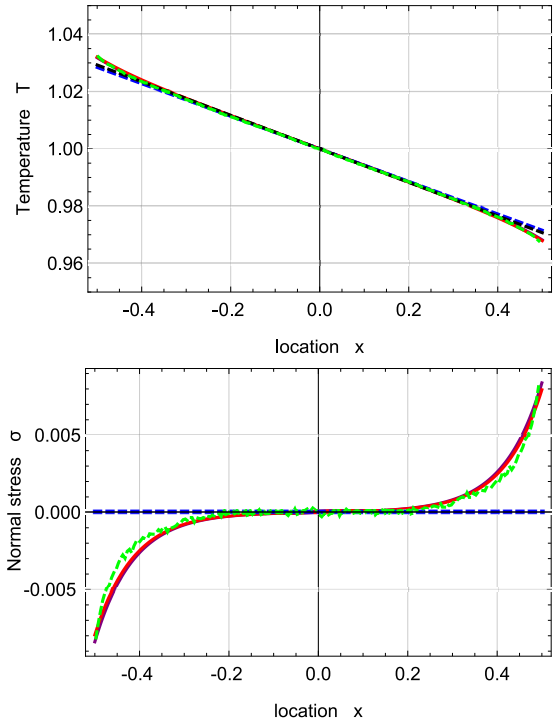

Figure 3.3: Temperature and normal stress profiles for Kn = 0.078 with $\Delta T = 0.05$ and $\Delta p = 0.05$: DSMC (symmetrized; green, dashed), R13 with PBC (purple), R13 with MBC (red), corrected NSF (blue, dashed), uncorrected NSF (black, dashed).

Both sets of boundary conditions for R13 reconstruct the DSMC results well but slightly underpredict the Knudsen layers both for temperature and normal stress. For the temperature profile they are in better agreement with DSMC than the two NSF solutions. For both Kn = 0.078 and Kn = 0.235 one notes the significant temperature jumps at the boundaries.

Additionally to temperature and normal stress profiles we seek to get insight into the three integration constants velocity V_0, conductive heat flux q_0 and Knudsen layer amplitude A, depending on the Knudsen number. The three variables are plotted over $\mathrm{Kn} = \{0, 1.0\}$ in Fig. 3.5. Sign of velocity V_0 and conductive heat flux q_0 are positive. That is, mass and conductive heat flux are transferred from warm to cold, i.e., they are transported at $x = -\frac{1}{2}$ into the system via evaporation and due to steady state the same amount of mass and conductive heat is transported at $x = \frac{1}{2}$ out of the system into the colder reservoir via condensation. R13 with PBC shows very good agreement with DSMC for V_0, q_0 for all Knudsen numbers. The PBC results for normal stress are better than those of MBC for $Kn < 0.4$. For higher Knudsen numbers both PBC and MBC fail to predict σ in precise agreement with DSMC. Again the normal stress

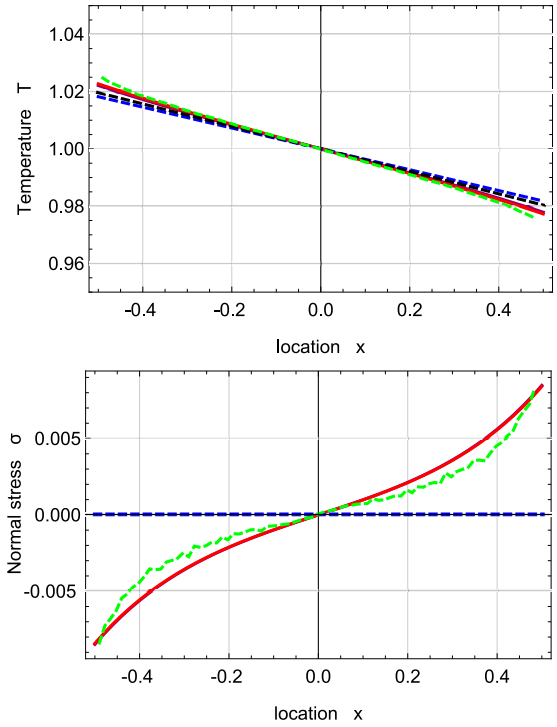

Figure 3.4: Temperature and normal stress profiles for Kn = 0.235 with $\Delta T = 0.05$ and $\Delta p = 0.05$: DSMC (symmetrized; green, dashed), R13 with PBC (purple), R13 with MBC (red), corrected NSF (blue, dashed), uncorrected NSF (black, dashed).

can not be predicted by NSF.

Interestingly for this PBC fit, Ytrehus' ratios are very similar to those of the MBC, i.e., 0.35% (PBC) and 0.74% (MBC) deviation for α_p and 10.33% (PBC) and 10.44% (MBC) for α_θ, see Table 3.3. Corrected NSF is under 1% deviation for both ratios. Uncorrected NSF shows zero deviation for α_θ and 6.18% for α_p. For Knudsen numbers larger than 0.235 the deviation between DSMC and the PBC becomes slightly larger for the temperature profile and stays similar for the normal stress profile. The temperature jump at the boundaries increases with increasing Knudsen number.

3.3.6 Fitting of the Onsager coefficients: inverted temperature profile

By adjusting the values for ΔT, Δp it can be shown that the sign of the conductive heat flux q_0 switches. This leads to an inverted temperature profile. The negative

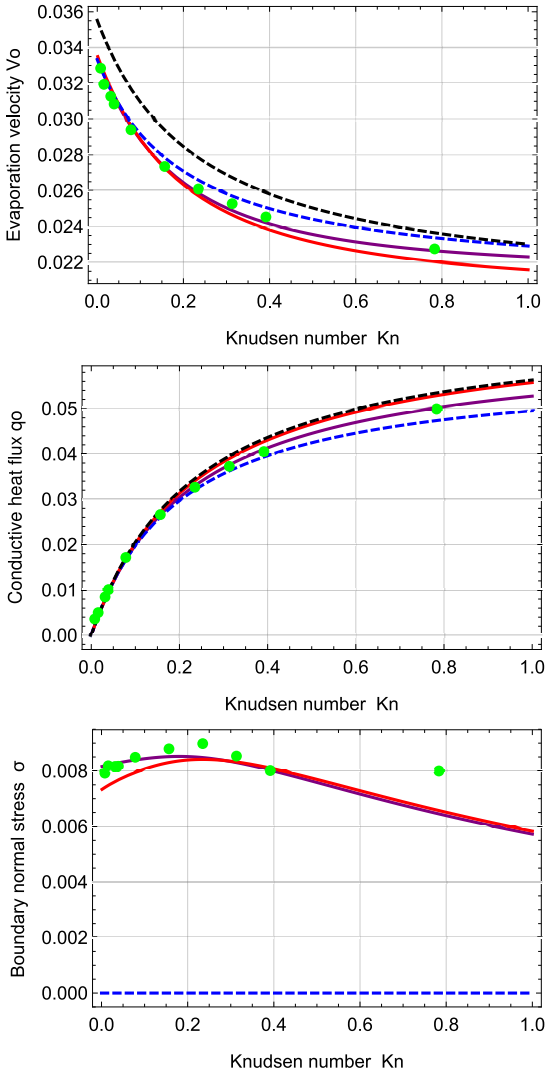

Figure 3.5: Evaporation velocity V_0, conductive heat flux q_0 and boundary normal stress σ_0 for standard temperature profile: DSMC (green, dots), R13 with PBC (purple), R13 with MBC (red), corrected NSF (blue, dashed), uncorrected NSF (black, dashed).

sign of q_0 indicates conductive heat transport from $x = \frac{1}{2}$ to $x = -\frac{1}{2}$, see Fig. 3.1. Though the second law is not violated since the overall heat transport is given with $Q = \rho V_0 h + q_0$ and the advective term $\rho V_0 h$ is dominant. Hence the overall heat Q is transported from hot to cold as expected. One notes that due to the reversed sign of the conductive heat flux, the necessary vaporization enthalpy is partly provided by the colder boundary. The liquid temperatures at the boundaries are set to $T_l^0 = 1.01$ and $T_l^1 = 0.99$. The respective saturation pressures follow as $p_{sat}(T_l^0) = 1.0752$ and

	a	b	c	d	e	f
PBC inverted profile	0.985	0.85	1.30	1.0	0.20	1.10

Table 3.4: Factors to adjust the Onsager coefficients of the PBC for the inverted profile.

	α_p	% to Ytrehus	α_θ	% to Ytrehus
PBC inverted profile	2.1373	0.56	0.4646	4.85
Ytrehus	2.1254	-	0.44311	-

Table 3.5: Solutions for Ytrehus' ratios and percentual deviation to Ytrehus' solution for inverted profile.

$p_{sat}(T_l^1) = 0.9248$. Therefore the evaporating material of the system is different to the standard profile. The small temperature difference between hot and cold boundaries and the large difference between the saturation pressures allows for a temperature jump large enough to reverse the sign of the conductive heat flux.

By fitting with trial and error, it was not possible to achieve proper results for the standard and inverted profiles at the same time. This is believed to be due to the fact that the evaporating material is different between standard and inverted case, since the saturation pressures are different. Therefore we present a fitting for the adjustable factors within the PBC for the inverted case which is given in Table 3.4. The ratios α_p,α_θ as well as the percentual deviation to Ytrehus' solution are presented in Table 3.5.

The temperature and stress profiles for Kn = 0.078 are given in Fig. 3.6. As comparison to the new fitting, a PBC solution, which uses the previous coefficients, is given as well (purple, dashed). R13 with PBC and MBC both overpredict the Knudsen layer at the interfaces. For the temperature profile, corrected NSF shows the best agreement with DSMC here. Normal stress is predicted well for PBC and MBC and is again zero for NSF. For Kn = 0.235 the overprediction of the R13 boundary conditions becomes so large that the profiles are not inverted anymore, as shown in Fig. 3.7. Note that it is possible to "turn" the PBC temperature profile to match DSMC, however this leads to worse results for other plots. In this case MBC shows slightly better results for temperature and normal stress profiles than MBC.

Fig. 3.8 illustrates evaporation velocity, conductive heat flux and normal boundary stress for the inverted profile. For velocity and conductive heat flux, R13 with PBC is in very good agreement with DSMC. In comparison to the standard profile, the normal boundary stress of PBC starts to differ from DSMC already earlier, i.e., for

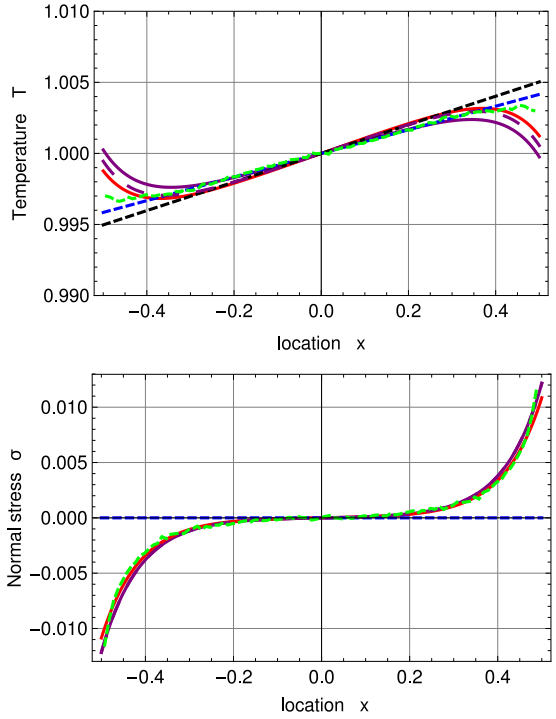

Figure 3.6: Inverted temperature and normal stress profiles for Kn = 0.078 with $\Delta T = 0.01$ and $\Delta p = 0.075$: DSMC (symmetrized; green, dashed), R13 with PBC (purple), R13 with PBC and previous fitting (purple, dashed), R13 with MBC (red), corrected NSF (blue, dashed), uncorrected NSF (black, dashed).

Kn > 0.1. Corrected NSF is in surprisingly good agreement with DSMC for Kn < 0.3 but fails to predict normal boundary stress. Except for temperature and normal stress profiles for Kn $= 0.235$, R13 with PBC shows the best agreement with DSMC for all discussed models here.

One notes that for this PBC fitting the deviation of α_θ to Ytrehus' solution becomes with 4.85% smaller than for the standard profile. For α_p the deviation stays small with 0.56%.

3.3.7 Impact of evaporation and accommodation coefficients

To gain a better understanding of the impact of evaporation and accommodation coefficients, the PBC shall be tested for the "standard temperature profile" of the previously discussed problem and a variety of ϑ, χ. Fig. 3.9 illustrates solutions of the PBC for Problem I, Fig. 3.1, together with the fitting from Table 3.2. The plots are based on $\chi = 0.1$ (Green), $\chi = 0.5$ (Red), $\chi = 1$ (Blue), $\vartheta = 0.1$ (solid), $\vartheta = 0.5$

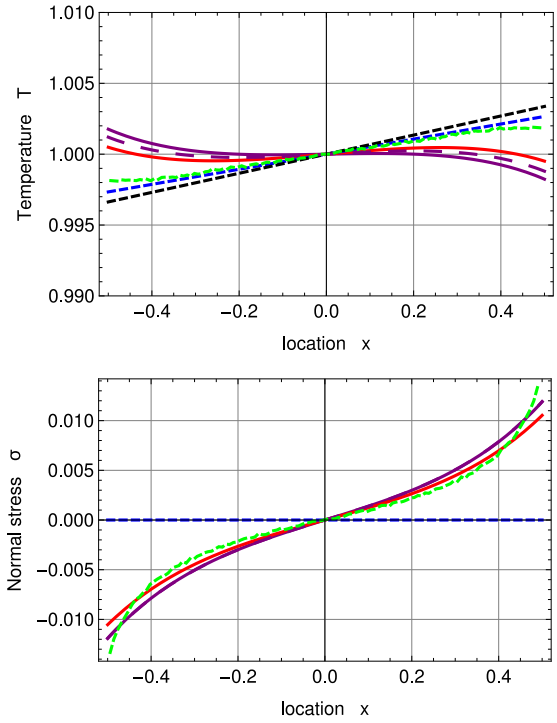

Figure 3.7: Inverted temperature and normal stress profiles for Kn = 0.235 with $\Delta T = 0.01$ and $\Delta p = 0.075$: DSMC (symmetrized; green, dashed), R13 with PBC (purple), R13 with PBC and previous fitting (purple, dashed), R13 with MBC (red), corrected NSF (blue, dashed), uncorrected NSF (black, dashed).

(dashed) and $\vartheta = 1$ (large, dashed). For $\vartheta = 1$, the solutions are independent of χ. Since the evaporation coefficient is defined over the condensation coefficient, this may be explained due to the fact that for the condensation coefficient being unity, no reflection occurs, all vapor molecules hitting the liquid interface are condensed. The largest temperature jump between gas and boundary is found for $\vartheta = 0.1$ and $\chi = 0.1$ and the smallest for $\chi = 1$.

The stress profile seems to be dependent, mainly on the evaporation coefficient. The accommodation coefficient has a small impact only for $\vartheta = 0.5$. The largest stress can be found for $\vartheta = 1$. Evaporation velocity V_0, conductive heat flux q_0 and boundary normal stress σ for various values of ϑ and χ are depicted in Fig. 3.10. The results of V_0 and σ seem to be almost independent of χ, except for $\vartheta = 0.5$, where χ has a small impact. Interestingly, both ϑ and χ have a large influence on q_0.

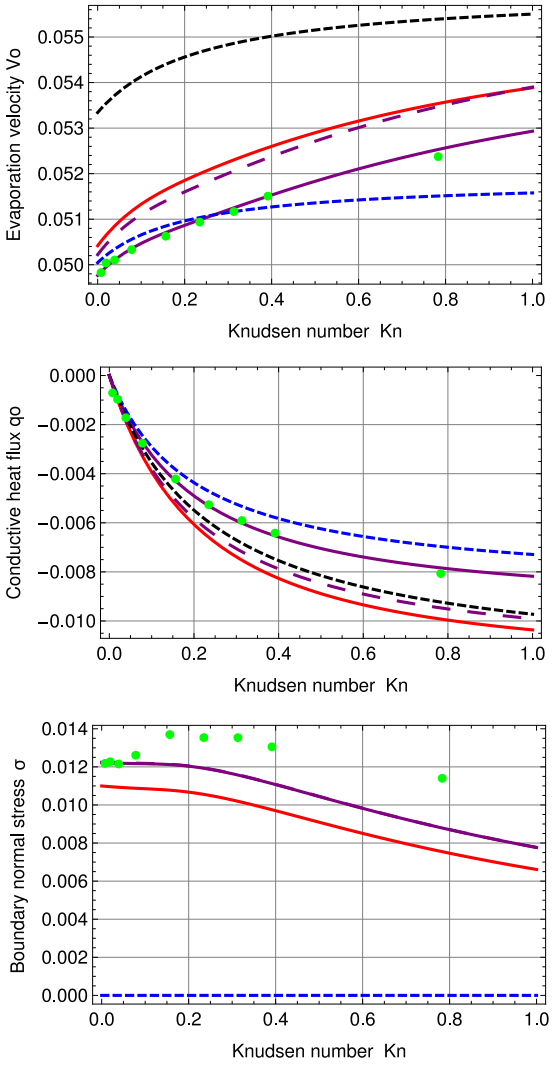

Figure 3.8: Evaporation velocity V_0, conductive heat flux q_0 and boundary normal stress σ_0 for inverted temperature profile: DSMC (green, dots), R13 with PBC (purple), R13 with PBC and previous fitting (purple, dashed), R13 with MBC (red), corrected NSF (blue, dashed), uncorrected NSF (black, dashed). Note: For σ, the two PBC solutions are represented by the solid, purple curve.

3.3.8 Notes on the meaning of the individual Onsager coefficients of the normal fluxes

The fittings used in the Tables 3.2 and 3.4 are based on a trial and error procedure, in which the factors $a - f$ in the Onsager coefficients (3.31-3.36) are individually adjusted. Due to symmetry of the Onsager matrix, six independent parameters need to be determined. The tuning of the Onsager coefficients one by one gives an insight

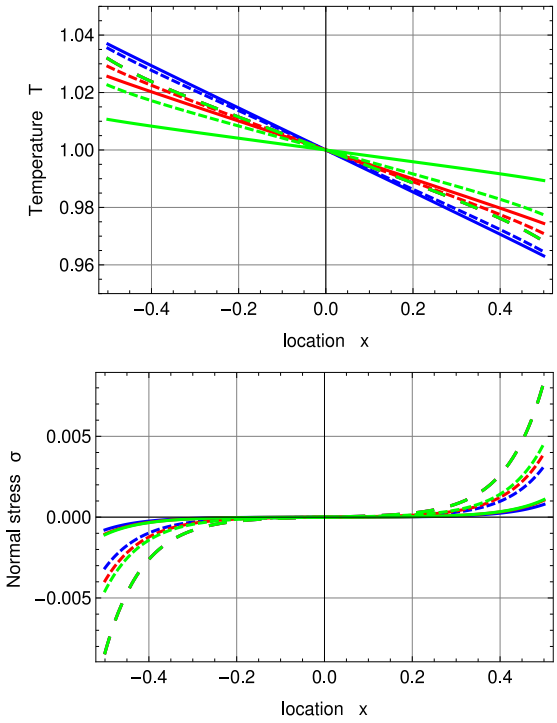

Figure 3.9: PBC temperature and normal stress profiles for Kn = 0.235 and various evaporation and accommodation coefficients: $\chi = 0.1$ (Green), $\chi = 0.5$ (Red), $\chi = 1$ (Blue), $\vartheta = 0.1$ (solid), $\vartheta = 0.5$ (dashed), $\vartheta = 1$ (large, dashed). Note: For $\vartheta = 1$, the large, dashed, green curve represents all three solutions.

into what outcome they influence. One notes however, that due to the coupling within the Onsager matrix in Eq. (3.28), the individual Onsager coefficient impacts multiple fluxes. The following is an attempt to determine some trends, which were observed during the fitting procedure.

Since λ_0 appears only in the equation for the normal velocity, it has a strong impact on V_0 and no impact on the conductive heat flux q_0. Apparently it has no impact on boundary normal stress σ. Temperature and stress profiles appear to be independent of λ_0 as well. The coefficient λ_1 has a big impact on V_0 and q_0 and a small impact on σ. It has a major impact on the temperature profile and a smaller impact on the stress profile. λ_2 strongly influences V_0 and σ and slightly q_0. Since λ_2 does not appear in the equation for q_0, this is expected. It has an impact on temperature and stress profiles but with clear emphasis on the stress profile.

The coefficient λ_3 seems to play a key role in the fitting. Even though it appears only in the equation for V_0, it has not only a strong impact on the magnitudes and slopes of V_0, but also on those of q_0. It slightly impacts σ as well. Regarding the

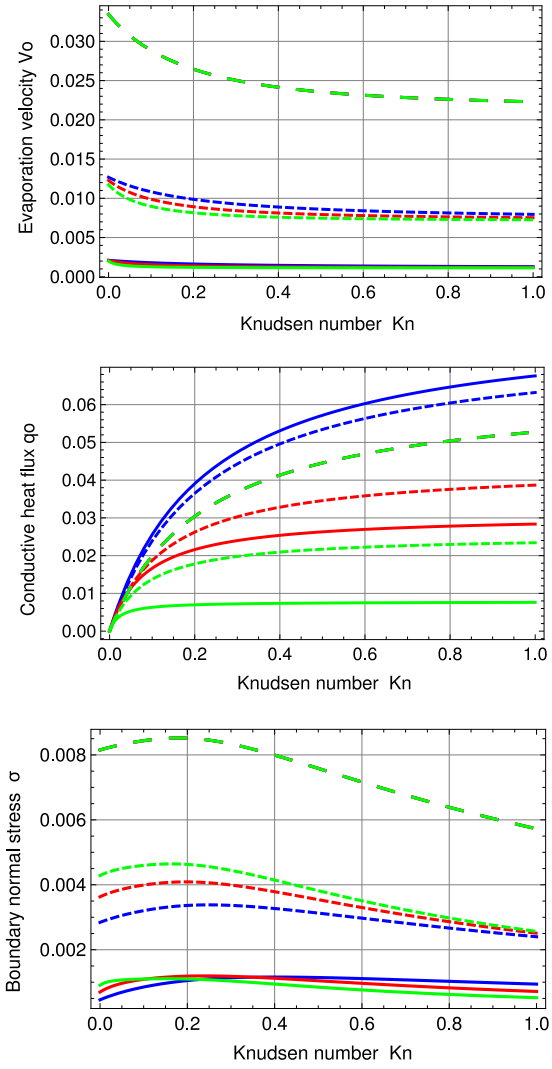

Figure 3.10: PBC evaporation velocity V_0, conductive heat flux q_0 and boundary normal stress σ_0 for standard temperature profile and various evaporation and accommodation coefficients: $\chi = 0.1$ (Green), $\chi = 0.5$ (Red), $\chi = 1$ (Blue), $\vartheta = 0.1$ (solid), $\vartheta = 0.5$ (dashed), $\vartheta = 1$ (large, dashed). Note: For $\vartheta = 1$, the large, dashed, green curve represents all three solutions.

profiles, λ_3 seems to impact only the temperature. The Onsager coefficient λ_4 mainly impacts σ, but also V_0, q_0 and both profiles, with stronger impact on the stress profile, as expected. λ_5 appears only in the equation for the normal component of the higher moment m_{nnn}. The coefficient has a strong impact on σ, a medium impact on V_0 and no impact on q_0. It influences the stress profile significantly and the temperature profile slightly. After these dependencies were established, several rounds of fitting were done, until a reasonable fitting was obtained.

Chapter 4

Evaporation in Numerical Two-Dimensional Steady-State Simulation

4.1 R13 with Phenomenological Onsager boundary conditions in numerical simulation

It shall be shown that the applicability of R13 with PBC (Phenomenological Boundary Conditions) is not limited to one-dimensional systems. A numerical solver for 2-D geometries, written in C++ by Torrilhon [27], is used in this chapter to solve the linear R13 equations with the PBC for evaporation. As comparison, simplified NSF (Navier-Stokes-Fourier) is solved with the same code. The program from Torrilhon allows for generic implementation of macroscopic transport equations. The numerical solver relies on a discontinuous Galerkin (DG) method which utilizes finite elements to discretize the system. Here the code is extended by implementing the evaporation boundary conditions, previously derived in Chap. 3.

The PBC for R13, given in Eqs. (3.28-3.30), are adjusted by using data for Maxwell molecules out of Table 3.1 and read

$$-\lambda_0\rho + v_x^g + (-\lambda_0 - \lambda_1)\,T^g + \left(-\lambda_0 - \frac{3}{4}\lambda_2 - \frac{2}{5}\lambda_1\right)\sigma_{xx} - \frac{1}{5}\lambda_1 R_{xx} = \lambda_1 T^l + \lambda_0 p_{sat}(T^l)\ , \tag{4.1}$$

	Evaporation/condensation	Wall with energy transfer	Inflow/outflow
λ_0	$a_0\vartheta_2$	0	$1/10^{-5}$
λ_1	$-\frac{1}{2}b_0\vartheta_2$	0	0
λ_2	$-\frac{2}{5}c_0\vartheta_2$	0	0
λ_3	$2d_0\chi_2$	$2d_0\vartheta_2$	$1/10^{-5}$
λ_4	$-\frac{2}{5}e_0\chi_2$	$-2e_0\vartheta_2$	0
λ_5	$f_0\left(\frac{52}{25}\chi_2+\frac{4}{15}\vartheta_2\right)$	$2f_0\vartheta_2$	0
ζ_0	$a_1\chi_2$	$a_1\vartheta_2$	1.0
ζ_1	$-b_1\chi_2$	$-b_1\vartheta_2$	1.0
ζ_2	$13c_1\chi_2$	$c_1\vartheta_2$	1.0
κ_0	$2a_2\chi_2$	$2a_2\vartheta_2$	1.0

Table 4.1: Adjustment of the Onsager coefficients to gain evaporation boundary conditions, wall boundary conditions and inflow boundary conditions.

$$-\lambda_1\rho+(-\lambda_1-\lambda_3)\,T^g+\left(-\lambda_1-\frac{3}{4}\lambda_4-\frac{2}{5}\lambda_3\right)\sigma_{xx}+q_x^g-\frac{1}{5}\lambda_3R_{xx}=\lambda_3T^l+\lambda_1p_{sat}(T^l)\ , \tag{4.2}$$

$$-\lambda_2\rho+(-\lambda_2-\lambda_4)\,T^g+\left(-\lambda_2-\frac{3}{4}\lambda_5-\frac{2}{5}\lambda_4\right)\sigma_{xx}+m_{xxx}-\frac{1}{5}\lambda_4R_{xx}=\lambda_4T^l+\lambda_2p_{sat}(T^l)\ , \tag{4.3}$$

$$-\zeta_0v_y+\sigma_{xy}+\left(-\frac{2}{5}\zeta_0-\frac{1}{5}\zeta_1\right)q_y-\zeta_0m_{xxy}=0\ , \tag{4.4}$$

$$-\zeta_1v_y+\left(-\frac{2}{5}\zeta_1-\frac{1}{5}\zeta_2\right)q_y-\zeta_1m_{xxy}+R_{xy}=0\ , \tag{4.5}$$

$$-\frac{1}{2}\kappa_0\sigma_{yy}+m_{xyy}=0\ . \tag{4.6}$$

Since for wall-vapor interfaces the DG-code uses a normal vector n pointing from vapor into the direction of the wall, the sign of T^l, $p_{sat}(T^l)$, v_x, q_x^g, m_{xxx}, σ_{xy}, R_{xy} and m_{xyy} is switched. The liquid phase is not solved and therefore can be treated in the same manner as a wall, which allows for mass transfer. Adjustment of the Onsager coefficients allows to derive other boundary conditions such as wall with energy transfer or inflow/outflow. Table 4.1 gives an overview about these modifications. The factors being used are given as

$$\chi_2=\sqrt{\frac{2}{\pi}}\frac{\vartheta+\chi(1-\vartheta)}{2-\vartheta-\chi(1-\vartheta)}\ ,\qquad \vartheta_2=\sqrt{\frac{2}{\pi}}\frac{\vartheta}{2-\vartheta}\ . \tag{4.7}$$

For an adiabatic wall (fully specular reflective) all Onsager coefficients are set to zero, which leads to $v_x^g=q_x^g=m_{xxx}=\sigma_{xy}=R_{xy}=m_{xyy}=0$. The Onsager

	Evaporation/condensation	Wall with energy transfer	Inflow/outflow
a_0	0.975	–	–
b_0	0.875	–	–
c_0	1.0	–	–
d_0	1.1	0.872	–
e_0	0.7	0.872	–
f_0	1.05	1.0	–
a_1	1.0 (Not fitted)	0.9143	1.0 (Not fitted)
b_1	1.0 (Not fitted)	0.9143	1.0 (Not fitted)
c_1	1.0 (Not fitted)	1.0	1.0 (Not fitted)
a_2	1.0 (Not fitted)	1.0 (Not fitted)	1.0 (Not fitted)

Table 4.2: Adjustable coefficients within Onsager coefficients for R13.

	Evaporation/condensation	Wall with energy transfer	Inflow/outflow
p_{sat}	p_{evap}	–	$\pm p_{flow}$
T_l	T_{evap}	T_w	T_{flow}

Table 4.3: Overview input parameters.

coefficients for a wall with energy transfer are taken from Ref. [21]. The adjustable coefficients within the Onsager coefficients for the different boundaries are set as in Table 4.2.

Note: The evaporation/condensation coefficients $a_0, ..., f_0$ are based on a fitting as in Problem I (Chap. 3), however different definitions of the Knudsen number between DSMC and R13 where used. Therefore a small error is introduced here. For evaporation/condensation the coefficients a_1, b_1, c_1 and a_2 are not fitted and set to unity. The adjustable coefficients for a wall with energy transfer $d_0, ..., f_0$ and $a_1, ..., c_1$ are taken from Ref. [21] and a_2 is set to unity. Depending on the boundary, different pressures and temperatures are assumed as depicted in Table 4.3.

From Tables 4.1 and 4.3 the inflow/outflow boundary conditions follow as

$$-(\rho + T^g) - \sigma_{xx} + \frac{v_x}{\lambda_0} = \pm p_{flow} \ , \tag{4.8}$$

$$-T^g - \frac{2}{5}\sigma_{xx} - \frac{1}{5}R_{xx} + \frac{q_x^g}{\lambda_3} = T_{flow} \ , \tag{4.9}$$

$$m_{xxx} = 0 \ , \tag{4.10}$$

$$-v_y - \frac{3}{5}q_y + \sigma_{xy} - m_{xxy} = 0 \ , \tag{4.11}$$

$$-v_y - \frac{3}{5}q_y - m_{xxy} + R_{xy} = 0 \ , \tag{4.12}$$

$$-\frac{1}{2}\sigma_{yy} + m_{xyy} = 0 \ . \tag{4.13}$$

Due to limited degrees of freedom when controlling variables at one boundary, the velocity v_x^g in Eq. (4.8) is removed. Since division by 0 is not defined, λ_0 is set to a value of much larger order of magnitude than v_x. In the same manner the heat flux q_x^g is removed. Hence, driving forces of the system which are controlled at both boundaries are pressure p_{flow} and temperature T_{flow}.

4.2 Navier-Stokes-Fourier with Onsager boundary conditions in numerical simulation

For obtaining a comparison to the R13 solutions for two-dimensional systems, Navier-Stokes-Fourier together with evaporation boundary conditions is solved here. For $\chi = \vartheta = 1$ and considering one-dimensional geometry, evaporation boundary conditions for NSF are given in Appendix D, see. (D.1). For 2- and 3-dimensional geometries an additional boundary condition is found in Ref. [18] and reads

$$\sigma_{xy}^g = -\frac{\vartheta + \chi(1-\vartheta)}{2 - \vartheta - \chi(1-\vartheta)}\sqrt{\frac{2}{\pi RT}}\left(pv_y^g + \frac{1}{5}q_y\right) \ . \tag{4.14}$$

Note that Eqs. (D.1) are simplified for 1-D geometry. Again by considering $\chi = \vartheta = 1$ and after full linearization and non-dimensionalization, Eq. (4.14) becomes

$$\sigma_{xy}^g = -\sqrt{\frac{2}{\pi}}\left(v_y^g + \frac{1}{5}q_y^g\right) \ . \tag{4.15}$$

For the DG-code one sets $T = -\frac{2}{3}T^*$, $q_x = -q_x^*$ and $q_y = -q_y^*$ and the evaporation boundary conditions for NSF (4.15) and (D.1) follow as

$$\rho - \sqrt{2\pi}r_{11}v_x^g - \frac{2}{3}T^* + \sqrt{2\pi}r_{12}q_x^* = -p_{sat} \ , \tag{4.16}$$

$$-\sqrt{2\pi}r_{21}v_x^g - \frac{2}{3}T^* + \sqrt{2\pi}r_{22}q_x^* = -T^l \ , \tag{4.17}$$

$$\sqrt{\frac{2}{\pi}}v_y^g - \sigma_{xy}^g - \frac{1}{5}\sqrt{\frac{2}{\pi}}q_y^* = 0 \ . \tag{4.18}$$

A corrected Onsager matrix for r_{11}, r_{12} and r_{22} which is used in the DG-code is given in (D.3). For a wall with energy transfer, (4.16-4.18) reduce to

$$v_x^g = 0 \ , \tag{4.19}$$

$$-\frac{2}{3}T^* + \sqrt{2\pi}r_{22}q_x^* = -T^l \ , \tag{4.20}$$

$$\sqrt{\frac{2}{\pi}}v_y^g - \sigma_{xy}^g - \frac{1}{5}\sqrt{\frac{2}{\pi}}q_y^* = 0 \ . \tag{4.21}$$

For an adiabatic wall (fully specular reflective) the trivial boundary conditions read

$$v_x^g = q_x^* = \sigma_{xy}^g = 0 \ . \tag{4.22}$$

The inflow/outflow b.c. used for NSF are given as

$$p_{sat} = -\rho + \frac{2}{3}T^* + \varepsilon\sqrt{2\pi}r_{11}v_x^g - \varepsilon\sqrt{2\pi}r_{12}q_x^* \ , \tag{4.23}$$

$$T^l = \frac{2}{3}T^* + \varepsilon\sqrt{2\pi}r_{21}v_x^g - \varepsilon\sqrt{2\pi}r_{22}q_x^* \ , \tag{4.24}$$

$$\sqrt{\frac{2}{\pi}}v_y^g - \sigma_{xy}^g - \frac{1}{5}\sqrt{\frac{2}{\pi}}q_y^* = 0 \ , \tag{4.25}$$

with $\varepsilon = 10^{-5}$ as factor of low order of magnitude to remove v_x^g and q_x^*. For the input parameters, Table 4.3 is used.

4.3 Results for two-dimensional simulation for R13 and NSF

4.3.1 Testing of the numerical simulation in quasi one-dimensional system

Before using the R13 and NSF-equations in a two-dimensional geometry they shall be tested and compared with analytical solutions from Problem I (Sec. 3.3.3). The analytical solutions for R13 with PBC and NSF with PBC are given in Eqs. (3.52-

3.54) and (3.55-3.56) respectively. To obtain a standard temperature profile with non-reversed heat flux, the driving forces at the boundaries are set as in (Sec. 3.3.5) to $T_l^0 = p_{sat}(T_l^0) = 1.05$ and $T_l^1 = p_{sat}(T_l^1) = 0.95$. All results use $\vartheta = \chi = 1$ in the following. In contrast to Sec. 3.3.5 the adjustable Onsager coefficients for evaporation being used are given in Table 4.2. For NSF the corrected Onsager matrix given in (D.3) is utilized. The numerical solutions for R13 and NSF model a quasi-one-dimensional system, depicted in Fig. 4.1 for R13.

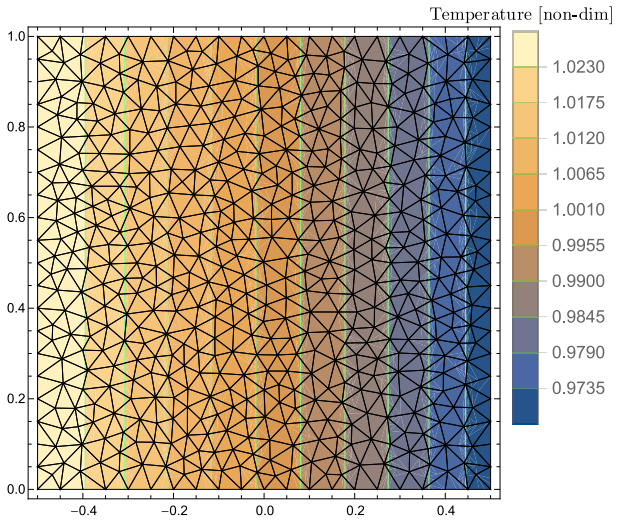

Figure 4.1: R13 in quasi one-dimensional system: Temperature distribution with grid mesh for Kn = 0.1.

The left and right boundaries are based on the full evaporation boundary conditions (4.1-4.6). Top and bottom are adiabatic walls with $v_x^g = q_x^g = m_{xxx} = \sigma_{xy} = R_{xy} = m_{xyy} = 0$. In Fig. 4.2 numerical solutions (blue line) are compared with analytical solutions (read line) for Kn = 0.1.

The agreement between numerical and analytical solutions for temperature and density profiles is flawless, therefore one can barely see the numerical solution underneath the analytical. One notes the non-linear behavior of R13 close to the boundaries due to Knudsen layers which can not be predicted by NSF.

4.3.2 Numerical solutions for two-dimensional channel-flow with four evaporating cylinders

The system of interest for the two-dimensional steady-state simulation is a channel with four evaporating cylinders, which is discretized as depicted in Fig. 4.3. The

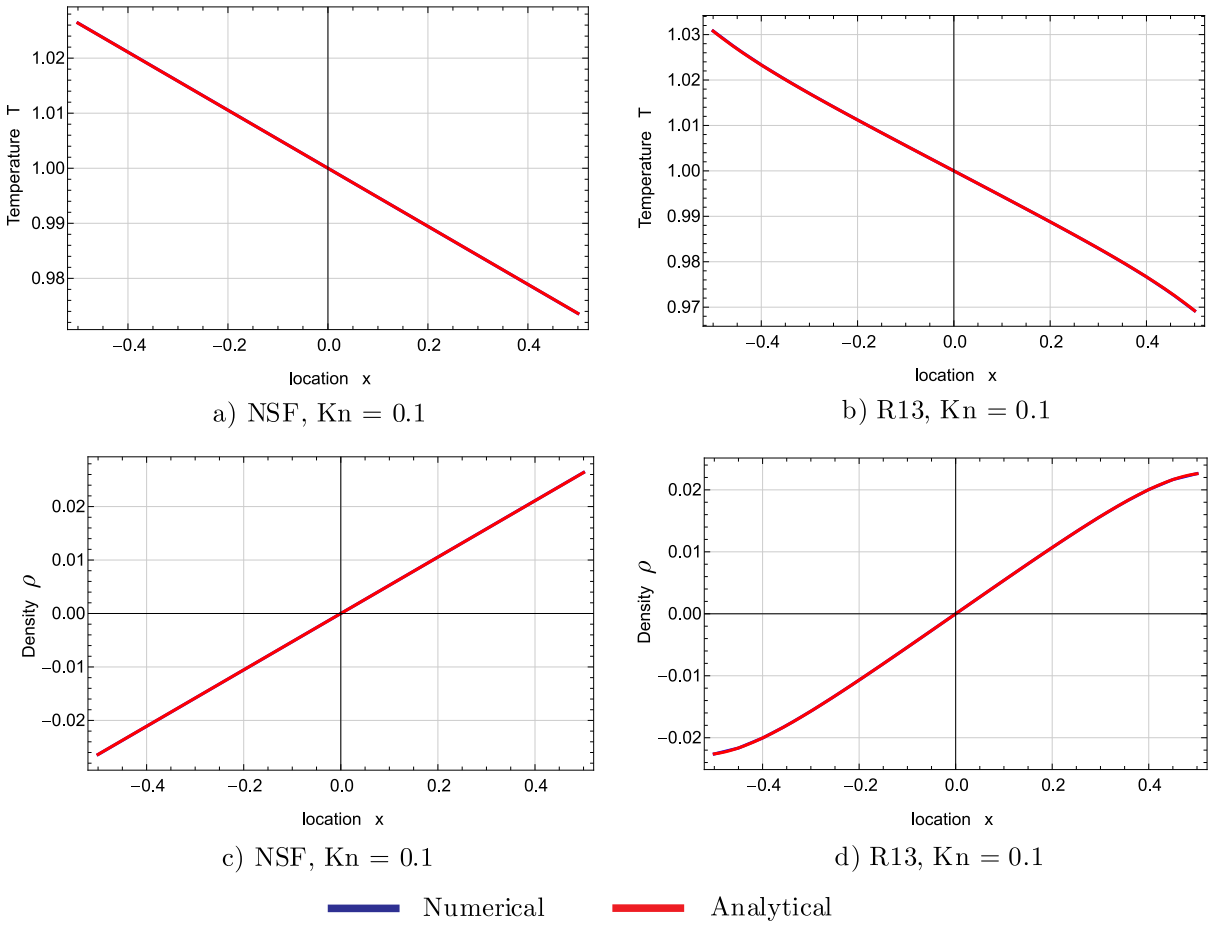

Figure 4.2: Analytical vs. numerical solutions of R13 and NSF in quasi one-dimensional system. Note: The numerical solution lies underneath the analytical solution.

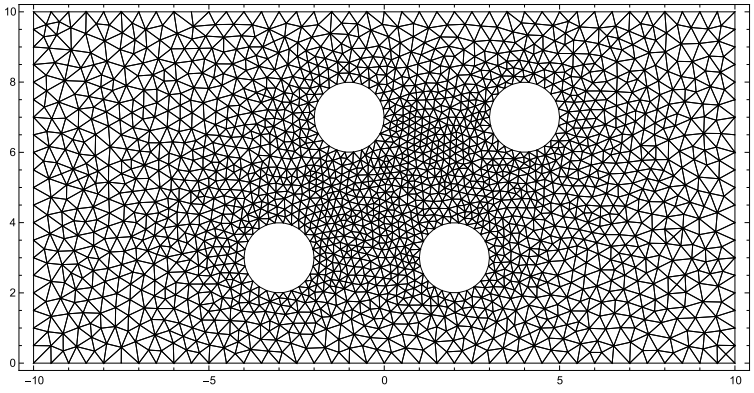

Figure 4.3: Grid of two-dimensional channel-flow with four evaporating cylinders.

left boundary is the inlet of the channel flow and the right boundary is the outlet.

	Evaporation/condensation	Wall with energy transfer	Inflow/outflow
p_{sat}	$p_{evap} = 0.2$	$-$	$\pm p_{flow} = 0.1$
T_l	$T_{evap} = 0.2$	$T_w = 0.2$	$T_{flow} = 0.2$

Table 4.4: Input parameters for two-dimensional channel flow with four evaporating cylinders.

For R13 inflow/outflow boundary conditions, the Eqs. (4.8-4.13) and for NSF, the Eqs. (4.23-4.25) are used. Top and bottom are walls which allow energy transfer, given with Table 4.1 for R13 and with Eqs. (4.19-4.21) for NSF. The cylinder walls use evaporation boundary conditions given by (4.1-4.6) with Table 4.1 for R13 and (4.16-4.18) for NSF. The input parameters, which are given in Table 4.4 are non-dimensional and describe the deviation from equilibrium. They are chosen in a way, that evaporation at the cylinders can be observed clearly.

The plots in Fig. 4.4 show pressure contours, superimposed by velocity streamlines, for R13 and NSF, for the three Knudsen numbers: Kn = $\{0.1, 0.5, 1\}$. For Kn = 0.1, the velocity streamlines are similar between R13 and NSF. The inflow of the left boundary collides with the evaporating flow, which leaves the two cylinders on the left-hand side. The largest flow velocity is observed in between the two cylinders on the right-hand side. For Kn = 0.5, the evaporation overcomes the inflow and leaves the system at the inlet of the channel. This interesting effect is observed for R13 and NSF, but with different flow behavior. For R13, the streamlines, which leave the inlet, have their origin mainly in the left bottom cylinder. The dominance of the left cylinder of R13 becomes even more apparent for Kn = 1. The NSF velocity streamlines at the inlet for Kn = $\{0.5, 1\}$ come almost equally from both left cylinders.

For Kn = 0.1, the pressure contours of R13 and NSF show very similar behavior. With increasing Kn, the R13-pressure contours on the right hand side of the diagrams disconnect from each other and become almost vertical for Kn = 1.

Also, for Kn = 1, significant differences between R13 and NSF are found for the temperature profiles, which are depicted in Fig. 4.5. The overall temperature around the four evaporting cylinders is much lower for NSF, than for R13. As can be seen by the conductive heat flux streamlines, the enthalpy of vaporization is provided by the boundaries, as in the previous simulations. The magnitude of the R13 heat flux, shows interesting peaks in between the two cylinders on the right-hand side for Kn = $\{0.5, 1\}$.

The large differences between R13 and NSF for Kn = $\{0.5, 1\}$ are likely due

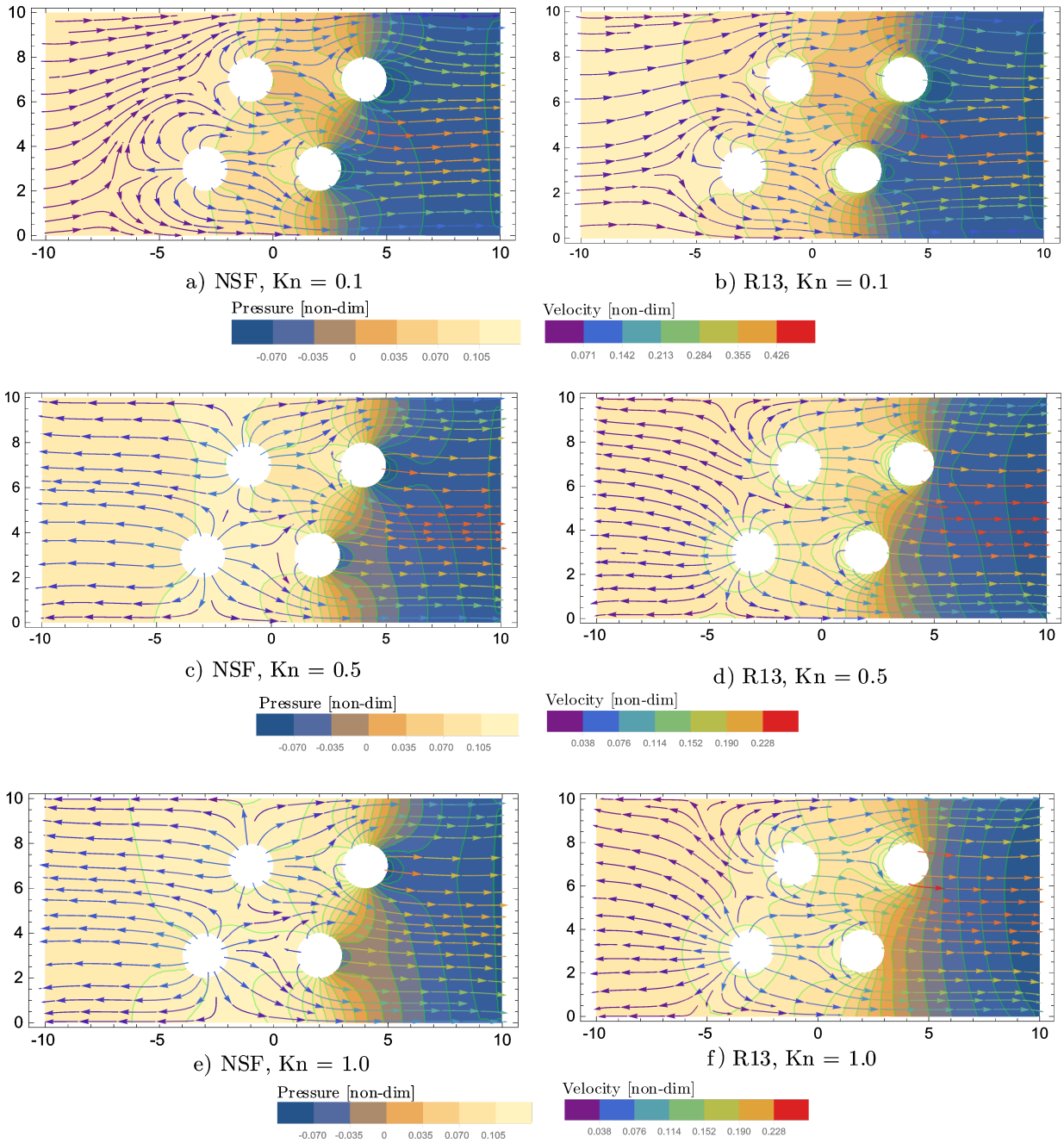

Figure 4.4: Pressure contours superimposed by velocity streamlines for two-dimensional channel-flow with four evaporating cylinders and various Knudsen numbers.

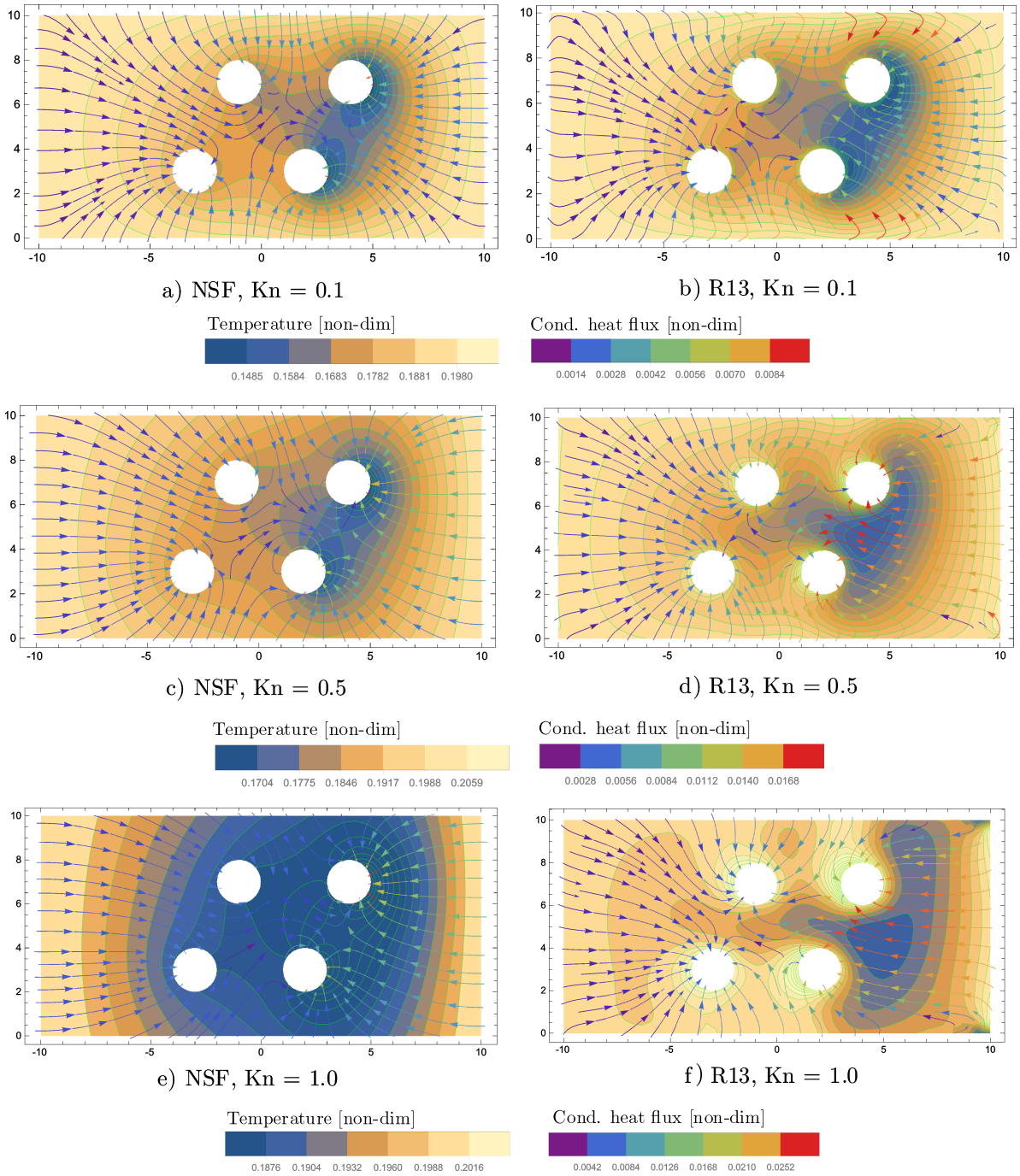

Figure 4.5: Temperature contours superimposed by cond. heat flux streamlines for two-dimensional channel-flow with four evaporating cylinders and various Knudsen numbers.

to rarefaction effects, which can not be captured by NSF. It has to be taken into account, as mentioned in Sec. 4.2, that simplified NSF boundary conditions are used here. Note that R13 is limited to flow regimes below Kn = 1 and can only describe a tendency here. For validation of the R13 results a reliable reference, such as from a DSMC simulation is necessary, which might be part of a future work.

Chapter 5

Conclusion

5.1 Summary and achievements

In Chap. 2 simplified Navier-Stokes-Fourier equations are considered to model slow evaporation in a non-steady and one-dimensional system. Driving force of evaporation is the controlled pressure on top of the vapor layer. Onsager boundary conditions are used for the interface between the two phases. The bulk equations are discretized by means of finite differences and solved explicitly. A matlab algorithm is suggested which is based on a dynamic mesh. Liquid and vapor heights are chosen to be 0.1mm respectively. This leads to a Knudsen number of Kn=0.01, which is just in the classical hydrodynamics regime. The simulation allows for calculation of all thermodynamic quantities and gives an insight into the physics of evaporation processes.

Based on the Onsager Theory which utilizes the second law of thermodynamics, evaporation boundary conditions (PBC) for the regularized R13 equations are derived in Chap. 3. The Onsager coefficients have been determined by following a process consisting of three steps. In the first step (Sec. 3.3.1) the boundary conditions are compared with previously discussed boundary conditions for evaporation (MBC), which represent an alternative approach for deriving boundary conditions for R13. Under the assumption of proper results for MBC in the Navier-Stokes-Fourier (NSF) regime and by keeping in mind that higher moments develop a significant impact only for higher Knudsen numbers, coefficients are being taken over from MBC to PBC so that the differences between the sets of boundary conditions lie mainly in the terms with higher moments [21]. The idea is to find boundary conditions which are just as reliable as MBC in the NSF regime and more accurate in the transition

regime. In the next step adjustable coefficients are suggested for the PBC. These coefficients are fitted by trial and error to DSMC data for the analytical solution of a finite one-dimensional system (Sec. 3.3.3). In the third step for finding meaningful Onsager coefficients the half space problem (Sec. 3.3.4) is solved analytically and ratios suggested by Ytrehus [24] are used to fine tune the coefficients. The overall agreement between PBC and DSMC (Sec. 3.3.5 and 3.3.6) has been shown to be better than for MBC or NSF.
The impact of the evaporation and accommodation coefficients is discussed in Sec. 3.3.7. In Sec. 3.3.8 it is explained, how the trial and error fitting gives an insight into the physical meaning of the individual Onsager coefficients.

In Chap. 4 the new evaporation/condensation boundary conditions are implemented into a code for the numerical solution of two-dimensional, steady-state problems. Results for Knudsen numbers of Kn=$\{0.1,0.5,1.0\}$ are obtained and compared to simplified Navier-Stokes-Fourier solutions. It is observed that with increasing Knudsen number, R13 shows different flow behavior than NSF.

5.2 Recommendations and future work

For the non-steady evaporation model in Chap. 2, one notes that the numerical approach chosen is restricted to the CFL criterion which limits the applicability for higher Knudsen numbers. In a future work we recommend to use an analytical method or implicit numerical method which is not bound to the CFL criterion. Also, for gaining an evaporation model with applicability in a flow regime further away from equilibrium, it might be of interest to solve the non-linearized Navier-Stokes-Fourier equations.

Due to lack of a mathematical approach, i.e., optimization algorithm, for fitting the Onsager coefficients in Chap. 3, it is uncertain if significantly better fittings for the presented problems are possible. This may be part of a future analysis. Even though NSF fails to predict normal stress for the presented problems, it shows surprisingly good results for low to moderate Knudsen Numbers. The advantage of R13 with PBC compared to NSF might be shown even more clearly in numerical simulations for complex geometries. The Onsager coefficients appear to be dependent on the evaporating material, which in the practical application becomes problematic. There-

fore we recommend an investigation considering the fitting of Onsager coefficients as function of the enthalpy of vaporization, which defines the material.

For the numerical simulation in Chap. 4, it is necessary to compare the results to a reliable reference, such as a DSMC solution, which shall be a future effort. Additionally it might be of interest to compare the numerical R13 results to those of a 26-moment method, see [28].

Bibliography

[1] A. Bejan, *Advanced Engineering Thermodynamics*. John Wiley & Sons, New Jersey, 2016.

[2] H. Struchtrup, *Thermodynamics and Energy Conversion*. Springer, Berlin Heidelberg, 2014.

[3] I. Mueller and W. Mueller, *Fundamentals of Thermodynamics and Applications*. Springer, Berlin Heidelberg, 2009.

[4] Y. A. Cengel, *Thermodynamics - An Engineering Approach*. McGraw-Hill, New York, 2008.

[5] P. Corbo, F. Migliardini, and O. Veneri, *Hydrogen Fuel Cells for Road Vehicles*. Springer, London, 2011.

[6] S. Srinivasan, *Fuel Cells - From Fundamentals to Applications*. Springer, New York, 2006.

[7] G. Karniadakis, A. Beskok, and N. Aluru, *Microflows and Nanoflows: Fundamentals and simulation*. Springer, New York, 2005.

[8] C. Cercignani, *Theory and application of the Boltzmann equation*. Scottish Academic Press, Edinburgh, 1975.

[9] G. Kremer, *An Introduction to the Boltzmann Equation and Transport Processes in Gases*. Springer, Berlin Heidelberg, 2010.

[10] G. A. Bird, *Molecular gas dynamics and the direct simulation of gas flows*. Oxford University Press, Oxford, 1994.

[11] H. Struchtrup, *Macroscopic Transport Equations for Rarefied Gas Flows - Approximation Methods in Kinetic Theory*. Springer, Berlin Heidelberg, 2005.

[12] M. Torrilhon, "Modeling nonequilibrium gas flow based on moment equations," *Annu. Rev. Fluid Mech.*, vol. 48, pp. 429–458, 2016.

[13] H. Struchtrup and M. Torrilhon, "Higher-order effects in rarefied channel flows," *Phys. Rev.*, vol. 78:046301, 2008.

[14] A. Rana, A. Mohammadzadeh, and H. Struchtrup, "A numerical study of the heat transfer through a rarefied gas confined in a micro cavity," *Continuum Mech. Thermodyn.*, vol. 27, pp. 433–446, 2015.

[15] A. Mohammadzadeh and H. Struchtrup, "Velocity dependent maxwell boundary conditions in dsmc," *Int. Journal of Heat and Mass Transfer*, vol. 87, pp. 151–160, 2015.

[16] H. Schlichting and K. Gersten, *Grenzschichttheorie (German).* Springer, Berlin Heidelberg, 2006.

[17] J. Caputa and H. Struchtrup, "Interface model for non-equilibrium evaporation," *Physica A*, vol. 390, pp. 31–42, 2011.

[18] H. Struchtrup, A. Beckmann, A. Rana, and A. Frezotti, "Evaporation boundary conditions for the r13 equations of rarefied gas dynamics," *Phys. Fluids*, vol. 29:092004, 2017.

[19] J. Sethian and P. Smereka, "Level set methods for fluid interfaces," *Ann. Rev. Fl. Mech.*, vol. 35, pp. 341–372, 2003.

[20] H. Struchtrup and M. Torrilhon, "Regularization of grad's 13 moment equations: Derivation and linear analysis," *Phys. Fluids*, vol. 15, pp. 2668–2680, 2003.

[21] A. Rana and H. Struchtrup, "Thermodynamically admissible boundary conditions for the regularized 13 moment equations," *Phys. Fluids*, vol. 28:027105, 2016.

[22] S. Kjelstrup, D. Bedeaux, E. Johannessen, and J. Gross, *Non-Equilibrium Thermodynamics for Engineers.* World Scientific, Singapore, 2010.

[23] S. Kjelstrup and D. Bedeaux, *Non-Equilibrium Thermodynamics of Heterogeneous Systems.* World Scientific, Singapore, 2008.

[24] T. Ytrehus, *Kinetic Theory Description and Experimental Results for Vapor Motion in Arbitrary Strong Evaporation*. Technical Note 112 (von Karman Institute for Fluid Dynamics), 1975.

[25] M. Bond and H. Struchtrup, "Mean evaporation and condensation coefficients based on energy dependent condensation probability," *Phys. Rev.*, vol. 70:061605, 2004.

[26] S. R. de Groot and P. Mazur, *Non-Equilibrium Thermodynamics*. North-Holland Publishing Company, Amsterdam, 1962.

[27] M. Torrilhon and N. Sarna, "Hierarchical boltzmann simulations and model error estimation," *Journal of Computational Physics*, vol. 342, pp. 66–84, 2017.

[28] A. Rana, D. Lockerby, and J. Sprittles, "Evaporation-driven vapour microflows: analytical solutions from moment methods," *Journal of Fluid Mechanics*, vol. 841, pp. 962–988, 2018.

[29] H. Struchtrup and M. Torrilhon, "H theorem, regularization, and boundary conditions for linearized 13 moment equations," *Phys. Rev. Lett.*, vol. 99:014502, 2007.

Appendix A

Derivation of Entropy Fluxes

Based on the incompressible Navier-Stokes-Fourier-equations, a reduced entropy flux Ψ_k^l for the liquid side of a liquid-gas interface shall be derived in the following. Here, the vapor is a monatomic ideal gas with specific heat $c_p = \frac{5}{2}R$ and the liquid is described as an incompressible simple liquid. The heat of vaporization at reference state T_0, $p_{sat}(T_0)$ is

$$h_{gl}^0 = h^g(T_0) - h^l(T_0) = \frac{5}{2}RT_0 - \left(c_l T_0 + \frac{p_{sat}(T_0)}{\rho_l} + h_0\right) , \tag{A.1}$$

with the enthalpies

$$h^l = c_l(T - T_0) + \frac{5}{2}RT_0 + \frac{p - p_{sat}(T_0)}{\rho_l} - h_{gl}^0 , \tag{A.2}$$

$$h^g = \frac{5}{2}RT . \tag{A.3}$$

The energy density of the liquid $\varepsilon^l = \rho_l u^l$, with u^l as the internal energy, is

$$\varepsilon^l = \rho_l\left(h^l - \frac{p}{\rho_l}\right) = \rho_l\left(c_l(T - T_0) + \frac{5}{2}RT_0 - \frac{p_{sat}(T_0)}{\rho_l} - h_{gl}^0\right) . \tag{A.4}$$

The entropy density $\eta^l = \rho_l s^l$ of the incompressible liquid is given as

$$\eta^l = c_l\rho_l \ln\frac{T^l}{T_0} - \frac{\rho_l}{T_0}h_{gl}^0 , \tag{A.5}$$

where the proper entropy difference at equilibrium state $\frac{\eta^v(T_0)}{\rho^v} - \frac{\eta^l(T_0)}{\rho_l} = \frac{h^0_{gl}}{T_0}$ was used. The conservation laws for mass, energy and entropy for a fluid are

$$\frac{\partial \rho}{\partial t} + \frac{\partial \rho v_k}{\partial x_k} = 0 \ , \tag{A.6}$$

$$\frac{\partial \left(\varepsilon + \frac{\rho}{2} v^2\right)}{\partial t} + \frac{\partial \left((\varepsilon + \frac{\rho}{2} v^2) v_k + q_k + p v_k + \sigma_{ik} v_i\right)}{\partial x_k} = 0 \ , \tag{A.7}$$

$$\frac{\partial \eta}{\partial t} + \frac{\partial \left(\eta v_k + \phi_k\right)}{\partial x_k} = \sigma_{gen} \ . \tag{A.8}$$

When one intends linearized balance laws, the entropy must be considered up to quadratic terms in deviations from equilibrium. To obtain a proper quadratic entropy, it is convenient to replace η by a linear combination $\widehat{\eta}$

$$\widehat{\eta} = \eta + \frac{5}{2} R\rho - \frac{1}{T_0}\left(\varepsilon + \frac{\rho}{2} v^2\right) \ , \tag{A.9}$$

which obeys the balance laws (A.6-A.8). Then, the reduced entropy balance reads

$$\frac{\partial \widehat{\eta}}{\partial t} + \frac{\partial \left(\widehat{\eta} v_k + \phi_k - \frac{1}{T_0}\left(p v_k + q_k + \sigma_{ik} v_i\right)\right)}{\partial x_k} = \Sigma_{gen} \ . \tag{A.10}$$

For deriving the entropy flux on the liquid side, incompressible Navier-Stokes-Fourier is used with $\phi_k = \frac{q^l_k}{T^l}$. Hence the reduced entropy flux can be read from (A.10) as

$$\Omega^l_k = \widehat{\eta}^l v^l_k + \frac{q^l_k}{T^l} - \frac{1}{T_0}\left(q^l_k + p^l v^l_k + \sigma^l_{ik} v^l_i\right) \ . \tag{A.11}$$

By using the equations of state for a liquid, (A.4,A.5) in (A.9) and after linearizing and non-dimensionalizing with (2.15) and (3.1), the reduced entropy density $\widetilde{\eta}^l$ assumes the form

$$\widetilde{\eta}^l = \frac{\widehat{\eta}^l}{R\rho_l} = \frac{p_{sat}\left(T_0\right)}{\rho_l R T_0} - \frac{c_l}{R}\frac{\left(\overline{T^l}\right)^2}{2} - \frac{1}{2}\left(\overline{v^l}\right)^2 \ . \tag{A.12}$$

The reduced entropy flux (dimensionless, linearized) on liquid side which, depending on evaporation or condensation, either enters or leaves the interface between liquid and vapor follows as

$$\Psi^l_k = \frac{\Omega^l_k}{\rho_0 R\sqrt{R T_0}} = -\overline{p^l v^l_k} - \overline{q^l_k}\,\overline{T^l} - \overline{\sigma^l_{ik} v^l_i} \ . \tag{A.13}$$

By considering R13 for the vapor phase, the entropy for the vapor can be found in the same manner, over a linear combination of (A.6-A.8). Though due to the higher moments, there are additional terms in the (dimensionless, linearized) reduced entropy density $\widetilde{\eta}^g$ and reduced entropy flux Ψ_k^g, see Ref. [29]:

$$\widetilde{\eta}^g = \overline{\eta_0} - \frac{\left(\overline{\rho^g}\right)^2}{2} - \frac{\left(\overline{v^g}\right)^2}{2} - \frac{3}{4}\left(\overline{T^g}\right)^2 - \frac{\varpi_2}{8}\left(\overline{\sigma^g}\right)^2 - \frac{2\theta_2}{25}\left(\mathrm{Pr}\right)^2\left(\overline{q^g}\right)^2 \ , \tag{A.14}$$

$$\Psi_k^g = -\overline{p^g}\overline{v_k^g} - \overline{q_k^g}\overline{T^g} - \overline{\sigma_{ik}^g v_i^g} - \frac{\varpi_3}{5}\,\mathrm{Pr}\,\overline{q_i^g \sigma_{ik}^g} - \frac{\varpi_2}{4}\overline{\sigma_{ij}^g}\,\overline{m_{ijk}} - \frac{2\theta_2}{25}\left(\mathrm{Pr}\right)^2\left(q_i^g\overline{R_{ik}} + \frac{\overline{\Delta}}{3}\overline{q_k^g}\right) . \tag{A.15}$$

The overbars which denote dimensionless deviations to the respective equilibrium state are neglected in Chap. 3.

Appendix B

Normal and Tangential Components

Within the process of deriving Onsager boundary conditions, it is desirable to decompose the tensors into their respective normal and tangential components. The normal component of a vector can be defined as

$$q_n = q_k n_k \ , \tag{B.1}$$

with its tangential component

$$\overline{q}_i = q_i - q_n n_i \ , \text{ with } \overline{q}_i n_i = 0 \ . \tag{B.2}$$

Similar one may define the components of a symmetric and trace-free tensor as [21]

$$\sigma_{nn} = \sigma_{rk} n_k n_r \ , \tag{B.3}$$

$$\overline{\sigma}_{ni} = \sigma_{ik} n_k - \sigma_{nn} n_i \ , \text{ with } \overline{\sigma}_{ni} n_i = 0 \ , \tag{B.4}$$

$$\widetilde{\sigma}_{ij} = \sigma_{ij} - \sigma_{nn}\left(\frac{3}{2} n_i n_j - \frac{1}{2}\delta_{ij}\right) - \overline{\sigma}_{ni} n_j - \widetilde{\sigma}_{nj} n_i \ , \text{ with } \widetilde{\sigma}_{ij} n_j = \widetilde{\sigma}_{kk} = 0 \ . \tag{B.5}$$

Here, σ_{nn} is the normal-normal component, $\overline{\sigma}_{ni}$ the normal-tangential component and $\widetilde{\sigma}_{ij}$ the tangential-tangential component. Similar for a symmetric and trace-free third order tensor, i.e., a 3-dimensional matrix one finds

$$m_{nnn} = m_{ijk} n_i n_j n_k \ , \tag{B.6}$$

$$\overline{m}_{nni} = m_{ijk} n_j n_k - m_{nnn} n_i \ , \text{ with } \overline{m}_{nni} n_i = 0 \ , \tag{B.7}$$

$$\widetilde{m}_{nij} = m_{ijk} n_k - m_{nnn} \left(\frac{3}{2} n_i n_j - \frac{1}{2} \delta_{ij} \right) - \overline{m}_{nni} n_j - \overline{m}_{nnj} n_i \ , \text{ with } \widetilde{m}_{nij} n_j = 0 \ . \tag{B.8}$$

Additionally one has:

$$\delta_{ij} \overline{m}_{nnj} n_i = \delta_{ij} \overline{\sigma}_{nj} n_i = \delta_{ij} \widetilde{m}_{nij} = 0 \ , \tag{B.9}$$

$$\delta_{ij} n_i n_j = n_j n_j = 1 \ . \tag{B.10}$$

Appendix C

Comparison of PBC vs. MBC for Non-Fitted Coefficients

For Maxwell molecules, the normal boundary conditions of PBC and MBC are compared with each other. The Onsager coefficients (3.31-3.36) are plugged into the PBC (3.28) while considering data for Maxwell molecules from Table. 3.1 and setting the adjustable coefficients $a = b = ... = f = 1$. The terms that are different between PBC and MBC are underlined, terms indicated with tilde appear in the MBC but not in the PBC. As mentioned in Chap. 3.3.1 there is a certain degree of freedom which coefficients to take over from the MBC, i.e., the here shown fitting is just one possibility. Our attempt is to have as many lower order terms such as p^g, σ_{nn} and $\left(T^g - T^l\right)$ equal between PBC and MBC but we seek to have differences in higher order terms, i.e., Δ and R_{nn}, see Chap. 3.3.1.

PBC:

$$V_n^g = \sqrt{\frac{2}{\pi}} \frac{\vartheta}{2-\vartheta} \left(p_{sat}\left(T^l\right) - p^g - \frac{1}{2}\sigma_{nn}^g + \frac{1}{2}\left(T^g - T^l\right) + \underline{\frac{1}{30}\Delta} + \underline{\frac{1}{10}R_{nn}} \right) \tag{C.1}$$

MBC:

$$V_n^g = \sqrt{\frac{2}{\pi}} \frac{\vartheta}{2-\vartheta} \left(p_{sat}\left(T^l\right) - p^g - \frac{1}{2}\sigma_{nn}^g + \frac{1}{2}\left(T^g - T^l\right) + \underline{\frac{1}{120}\Delta} + \underline{\frac{1}{28}R_{nn}} \right) \tag{C.2}$$

PBC:

$$q_n^g = -\sqrt{\frac{2}{\pi}}\frac{\vartheta+\chi(1-\vartheta)}{2-\vartheta-\chi(1-\vartheta)}\left(2\left(T^g-T^l\right)+\frac{1}{2}\sigma_{nn}^g+\underline{\frac{2}{15}}\Delta+\underline{\frac{2}{5}}R_{nn}\right)$$
$$-\frac{1}{2}\sqrt{\frac{2}{\pi}}\frac{\vartheta}{2-\vartheta}\left[p_{sat}\left(T^l\right)-p^g-\underline{\sigma_{nn}^g}\right] \quad \text{(C.3)}$$

MBC:

$$q_n^g = -\sqrt{\frac{2}{\pi}}\frac{\vartheta+\chi(1-\vartheta)}{2-\vartheta-\chi(1-\vartheta)}\left(2\left(T^g-T^l\right)+\frac{1}{2}\sigma_{nn}^g+\underline{\frac{1}{15}}\Delta+\underline{\frac{5}{28}}R_{nn}\right)$$
$$-\frac{1}{2}\sqrt{\frac{2}{\pi}}\frac{\vartheta}{2-\vartheta}\left(p_{sat}\left(T^l\right)-p^g-\underline{\frac{1}{2}}\sigma_{nn}^g+\frac{1}{2}\widetilde{(T^g-T^l)}+\widetilde{\frac{1}{120}}\Delta+\widetilde{\frac{1}{28}}R_{nn}\right) \quad \text{(C.4)}$$

PBC:

$$m_{nnn} = \sqrt{\frac{2}{\pi}}\frac{\vartheta+\chi(1-\vartheta)}{2-\vartheta-\chi(1-\vartheta)}\left(\frac{2}{5}\left(T^g-T^l\right)-\frac{7}{5}\sigma_{nn}^g+\underline{\frac{2}{75}}\Delta+\underline{\frac{2}{25}}R_{nn}\right)$$
$$-\frac{2}{5}\sqrt{\frac{2}{\pi}}\frac{\vartheta}{2-\vartheta}\left(p_{sat}\left(T^l\right)-p^g-\frac{1}{2}\sigma_{nn}^g\right) \quad \text{(C.5)}$$

MBC:

$$m_{nnn} = \sqrt{\frac{2}{\pi}}\frac{\vartheta+\chi(1-\vartheta)}{2-\vartheta-\chi(1-\vartheta)}\left(\frac{2}{5}\left(T^g-T^l\right)-\frac{7}{5}\sigma_{nn}^g+\underline{\frac{1}{75}\Delta-\frac{1}{14}}R_{nn}\right)$$
$$-\frac{2}{5}\sqrt{\frac{2}{\pi}}\frac{\vartheta}{2-\vartheta}\left(p_{sat}\left(T^l\right)-p^g-\frac{1}{2}\sigma_{nn}^g+\frac{1}{2}\widetilde{(T^g-T^l)}+\widetilde{\frac{1}{120}}\Delta+\widetilde{\frac{1}{28}}R_{nn}\right) \quad \text{(C.6)}$$

Appendix D

Onsager Boundary Conditions for Navier-Stokes-Fourier Equations

Here the Navier-Stokes-Fourier equations are used together with evaporation boundary conditions based on the Onsager theory. The Eqs. (2.35,2.36) are simplifications for full evaporation, $\vartheta = 1$, fully diffusive reflection, $\chi = 1$ and by considering one-dimensional heat and mass transfer only [17][18]. They are given in fully linearized form below

$$\begin{bmatrix} \frac{p_{sat}-p^g}{\sqrt{2\pi}} \\ \frac{\left(T^l-T^g\right)}{\sqrt{2\pi}} \end{bmatrix} = \begin{bmatrix} \widehat{r}_{11} & \widehat{r}_{12} \\ \widehat{r}_{21} & \widehat{r}_{22} \end{bmatrix} \begin{bmatrix} v_x^g \\ q_x^g \end{bmatrix} . \tag{D.1}$$

All variables are non-dimensional and linearized. The matrix of Onsager coefficients read [17][18]

$$\widehat{r}_{\alpha\beta} = \begin{bmatrix} \left(\frac{1}{\vartheta} - \frac{1}{2}\right) + \frac{1}{16} & \frac{1}{8} \\ \frac{1}{8} & \frac{1}{4} \end{bmatrix} . \tag{D.2}$$

Solutions based on (D.2) in Chap. (3.3) are referred to as uncorrected NSF. A correction can be found in kinetic theory which yields [17][18]

$$\widehat{r}_{\alpha\beta,corr} = \begin{bmatrix} \frac{1}{\vartheta} - 0.40044 & 0.126 \\ 0.126 & 0.291 \end{bmatrix} . \tag{D.3}$$